

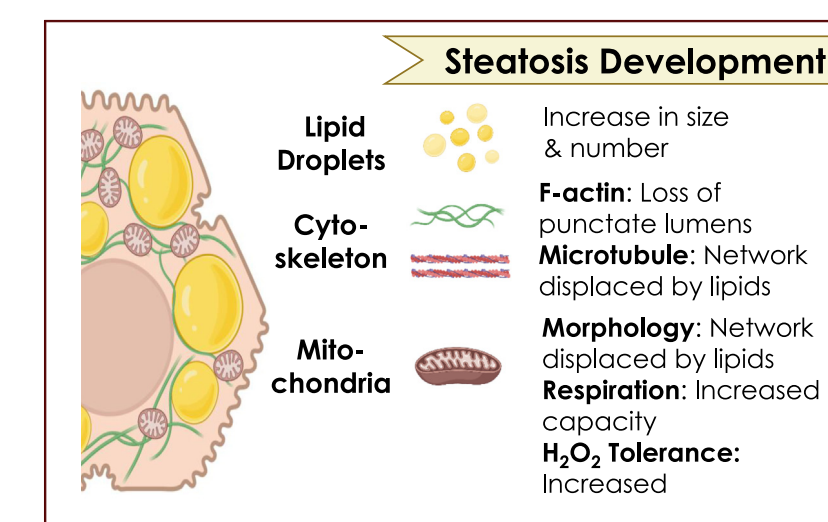
ORIGINAL RESEARCH

Alterations in Cytoskeleton and Mitochondria in the Development and Reversal of Steatosis in Human Hepatocytes



Letao Fan, ^{1,2,3} Aslihan Gokaltun, ^{1,2,3,4,5} Sarah Maggipinto, ^{1,3} Yoshinori Kitagawa, ^{3,6} Jeevendra Martyn, ^{3,6} Heidi Yeh, ² Basak E. Uygun, ^{1,2,3} Martin L. Yarmush, ^{1,2,3,7} and O. Berk Usta ^{1,2,3}

¹Center for Engineering in Medicine and Surgery, Massachusetts General Hospital, Harvard Medical School, Boston, Massachusetts; ²Department of Surgery, Massachusetts General Hospital, Boston, Massachusetts; ³Department of Scientific Research, Shriners Hospital for Children, Boston, Massachusetts; ⁴Department of Chemical and Biological Engineering, Tufts University, Medford, Massachusetts; ⁵Department of Chemical Engineering, Hacettepe University, Beytepe, Ankara, Turkey; ⁶Department of Anesthesiology, Critical Care and Pain Medicine, Massachusetts General Hospital, Boston, Massachusetts; and ⁷Department of Biomedical Engineering, Rutgers University, Piscataway, New Jersey



Reversal

Almost fully disappeared

F-actin: Punctate lumens restored

Microtubule: Intracellular distribution restored, decreased α-tubulin

Morphology: Elongated, pro-fusion **Respiration**: Increased capacity,

high proton leak

H₂O₂ Tolerance: Decreased, cells

sensitized to H₂O₂ treatment

cmgh CELLULAR AND MOLECULAR AND MOLECULAR AND MOLECULAR GASTROIGN GASTROIGN

SUMMARY

Mitochondrial injuries and alterations are well established in steatosis and nonalcoholic fatty liver disease. Nevertheless, little is known if such alterations also exist upon recovery. Here, we identified a cytoskeleton–mitochondrial pathway that predisposes hepatocytes to reactive oxygen species–induced death even upon the reversal of steatosis in vitro.

BACKGROUND & AIMS: Alterations in mitochondrial morphology and function and increased oxidative stresses in hepatocytes are well established in nonalcoholic fatty liver disease (NAFLD). Patients can undergo lifestyle changes, especially in earlier NAFLD stages, to reverse disease-induced phenotypes on a gross level. Yet, little is known about whether mitochondrial function and injuries recover upon reversal. Thus, we elucidated this question and interplays between the cytoskeletal network and mitochondria in the development and reversal of steatosis.

METHODS: We cultured primary human hepatocytes stably for 2 weeks and used free fatty acid supplementation to induce steatosis over 7 days and reversed steatosis by free fatty acid withdrawal over the next 7 days. We assessed cytoskeletal and mitochondrial morphologies using immunocytochemistry and confocal microscopy. We evaluated mitochondrial respiration and function via the Seahorse analyzer, in which we fully optimized reagent dosing specifically for human hepatocytes.

RESULTS: During early steatosis, intracellular lipid droplets displaced microtubules altering mitochondrial distribution, and disrupted the F-actin network, leading to loss of bile canaliculi in steatotic hepatocytes. Basal mitochondrial respiration, maximum respiratory capacity, and resistance to H_2O_2 -induced cell death also increased as an adaptative response. Upon reversal of steatosis, F-actin and bile canaliculi were restored in hepatocytes. Nevertheless, we observed an increase in elongated mitochondrial branches accompanied by decreases in α -tubulin expression, mitochondrial proton leak, and susceptibility to H_2O_2 -induced cell death.

CONCLUSIONS: Despite the restoration of cytoskeletons morphologically upon reversal of steatosis, the mitochondria in hepatocytes were impaired owing to early adaptative respiratory increase. Hepatocytes thus were highly predisposed to $\rm H_2O_2$ -induced cell death. These results indicate the persistence of potential health risks for recovering NAFLD patients. (Cell Mol Gastroenterol Hepatol 2023;16:243–261; https://doi.org/10.1016/j.jcmgh.2023.04.003)

Keywords: Nonalcoholic Fatty Liver Disease; Steatosis; Cytoskeleton; Mitochondria.

See editorial on page 321.

Nonalcoholic fatty liver disease (NAFLD) is one of the most complicated and widespread diseases that modern medicine has to face. ^{1,2} NAFLD is hallmarked by the accumulation of intracellular lipids independently of alcohol consumption. It encompasses a wide spectrum of progression stages from simple steatosis, nonalcoholic fatty liver, to nonalcoholic steatohepatitis (NASH), cirrhosis, and hepatocellular carcinoma. ^{3–5} Each stage is characterized differently and poses different threats to the patient's health and the treatment varies significantly. In recent years, NAFLD has been categorized as a vital component in the metabolic syndrome associated with obesity and insulin resistance, ^{6,7} and ranked as the most common chronic liver disease in the world. ^{8–10}

Because of its complexity, several competing hypotheses, interpreting the development and progression of NAFLD, evolved over time. These then led to the long-standing twohit hypothesis, which described the pathogenesis of NAFLD after its progression to different stages. The first hit was described as the accumulation of lipids, and the hypermetabolizing activity to process these lipids. This hypermetabolism was expected to promote oxidative stress and lipid peroxidation, resulting in the activation of downstream inflammatory and fibrotic pathways. Thus, the first hit was hypothesized to sensitize the liver to further insults (ie, the second hit which involves the activation of inflammation and fibrogenesis). 14 This second hit then initiates the progression to NASH and cirrhosis. More recently, as more characteristics of NAFLD pathogenesis—such as lipotoxicity, innate immune activation, and genetic susceptibility—were identified, a multiple hit hypothesis emerged, which described the interplay of these parallel pathways and molecular events better. 15,16 However, whether the multiple-hit hypothesis is the perfect interpretation for the development of NAFLD is unclear, leaving several gaps unfilled, such as the role of cytoskeletal interplay.

Despite differences in competing theories on the causality of different events during pathogenesis, a common feature in NAFLD is the alterations in mitochondrial function and structure. Increased mitochondrial respiratory capacity has been observed in patients and animal models of early stage NAFLD, such as simple steatosis. This compensatory increase reflects an adaptative response to increased lipid metabolism and gluconeogenesis in NAFLD to protect the liver from free fatty acid (FFA)-mediated toxicity. However, if the insults

from excessive lipid metabolism—such as oxidative stresses from β -oxidation and the tricarboxylic acid cycle—persist, this preventative adaptive mechanism will be disrupted and the mitochondrial respiratory capacity tumbles.²⁰ As the increased compensatory capacity is lost, the production of more reactive oxygen species (ROS) will not be balanced and will contribute further to mitochondrial damage in late-stage NAFLD.^{21,22} Abnormal morphology including swelling, crystalline inclusion, and a reduction in the number of mitochondria, 23,24 as well as decreased production of adenosine triphosphate (ATP), 25,26 have been reported in the pathophysiology of late-stage NAFLD, such as NASH. The mitochondrial impairment is potentially owing to oxidative DNA damage, 18 which is in line with reports of depletion and epigenetic changes in mitochondrial DNA in NASH patients and mouse models of NASH.^{27,28} However, whether the mitochondrial dysfunction results from interplay with other cellular components in the development of NAFLD remains unclear.

In general, the cellular mitochondrial network adapts and remodels rapidly in response to energy and metabolism demands via interaction with cytoskeletons.^{29,30} Among these, the microtubule cytoskeleton provides structural heterogeneity and aids in adaptive responsiveness for the mitochondria.31 Specifically, mitochondria translocate along the microtubular network to where the energy demand is high.32 This motility supported by the microtubules also is essential turnover and removal of aged and stressed mitochondria.33-35 The other cytoskeleton, F-actin, also facilitates the motility of the mitochondria³⁶ and regulates its intracellular distribution.37 More importantly, F-actin facilitates the fusion³⁸ and fission^{39–41} dynamics of mitochondria. The mitochondrial-cytoskeletal interaction and its vital role in maintaining fundamental cellular functions have been elucidated, but mainly in neurons^{29,31} and cardiomyocytes.⁴² The role of cytoskeletons has been reviewed regarding membrane transport and maintaining the polarization of the hepatocyte 43 and in the pathophysiology of alcohol-induced liver injury.⁴⁴

Alterations to mitochondrial structure and function thus are well documented in nonalcoholic fatty liver progression and pathogenesis. Nevertheless, the interaction of mitochondria and cytoskeleton in the parenchymal cells of the liver (ie, the hepatocytes), during the pathogenesis of NAFLD is not well

Abbreviations used in this paper: ATP, adenosine triphosphate; BODIPY, boron-dipyrromethene; DAPI, 4,6-diamidino-2-phenylindole; ECM, extracellular matrix; FCCP, p-trifluoromethoxy-phenylhydrazone; FFA, free fatty acid; GAPDH, glyceraldehyde-3-phosphate dehydrogenase; IC₅₀, median inhibitory concentration; MFF, mitochondrial fission factor; NAFLD, nonalcoholic fatty liver disease; NASH, nonalcoholic steatohepatitis; OCR, oxygen consumption rate; OPA1, optic atrophy-1; OXPHOS, oxidative phosphorylation; ROS, reactive oxygen species; Rot/ AA, rotenone and antimycin A; TOMM20, translocase of the outer mitochondrial membrane complex subunit 20; 7F, hepatocytes cultured for 7 days in medium supplemented with oleic acid and palmitic acid; 7F7L, hepatocytes cultured in fatty medium for the first 7 days followed by culture in the lean medium for the next 7 days; 7L, hepatocytes cultured cultured for 7 days in regular (lean) medium.

Most current article

© 2023 The Authors. Published by Elsevier Inc. on behalf of the AGA Institute. This is an open access article under the CC BY-NC-ND license (http://creativecommons.org/licenses/by-nc-nd/4.0/).

2352-345X

https://doi.org/10.1016/j.jcmgh.2023.04.003

understood. Furthermore, it is not well characterized whether the early alterations to mitochondria and the cytoskeletons observed in steatosis persist when the steatosis is reversed by different interventions. Such interventions, through lifestyle and dietary changes or therapeutics, 45 can achieve a morphologically healthier tissue phenotype of a gross level. Significant improvements in liver histology are seen in overweight and obese NAFLD patients after a 5%-10% weight loss. 46,47 Yet, little is known about whether alterations to the mitochondria and the cytoskeletons can persist in patients even after such successful interventions. We hypothesized that such alterations might indeed be persistent upon reversal of major NAFLD phenotypic markers. Importantly, these persistent alterations, especially to the mitochondria, may potentially put recovering NAFLD patients at increased risk of injury by especially oxidative insults, among other insults.

Accordingly, here, we developed an in vitro culture model to stably culture primary human hepatocytes for up to 2 weeks. We then sought to characterize structural alterations in mitochondria and cytoskeletal networks and functional alterations in mitochondria during the development of steatosis and its subsequent reversal. To this end, we have used an FFA cocktail supplementation to the standard culture medium to induce steatosis over 7 days, and withdrawal of this cocktail over the next 7 days to reverse the steatotic phenotype. Subsequently, we have assessed the quantity, morphology, and distribution of the cytoskeletons and mitochondria using immunohistochemistry, confocal imaging, and Western blot. We also assessed the mitochondrial respiratory dynamics and the susceptibility of hepatocytes to oxidative stress-induced death both in the steatotic stage and after reversing such phenotypes. Specifically, we used a Seahorse XF HS mini Analyzer to assess different respiratory characteristics in which we first fully optimized the dosing of different reagents for use with primary human hepatocytes. We then conducted an H₂O₂ dose-response study to assess the capacity of steatotic and reversed hepatocytes to manage oxidative stress-induced injuries.

We found that substantial alterations to cytoskeletons, especially the F-actin network, upon the development of steatosis were resolved upon the reversal of steatosis. In contrast, we observed an increase in elongated mitochondrial branches accompanied by increases in α -tubulin expression, mitochondrial proton leak, and susceptibility to $\rm H_2O_2$ -induced cell death. These results indicate that some of the mitochondrial and cytoskeletal injuries to liver tissue may persist upon reversal of steatosis, and possibly in recovering NAFLD patients who undergo different interventions to resolve disease-related phenotypes. Furthermore, such injuries also might lead to increased susceptibility to cell and tissue death by oxidative stresses owing to internal and external agents, and cellular processes.

Results

Induction and Reversal of Steatosis in Human Hepatocytes

Our study consisted of 4 different groups: 2 time-control groups and 2 experimental groups for the induction and

reversal of steatosis. The time courses for these groups are shown in Figure 1A. Hepatocytes were cultured in the regular (lean) medium for 7 (7L) and 14 (14L) days as time controls. Steatosis was induced by culturing hepatocytes in a medium supplemented with FFAs (oleic acid and palmitic acid) for 7 days (7F) for the first experimental group, referred to as the steatosis group. The reversed steatosis group (7F7L), on the other hand, was cultured in the fatty medium for the first 7 days followed by culture in the lean medium for the next 7 days.

We characterized the morphology and the extent of lipid accumulation in our studies via imaging. Specifically, we used both phase-contrast imaging (Figure 1B, upper panels) and fluorescent imaging where we used boron-dipyrromethene (BODIPY) for lipid droplets and counterstain 4,6diamidino-2-phenylindole (DAPI) for delineating the cell nuclei (Figure 1B, lower panels). We quantitated both the size and number of droplets (Figure 1C). The 7L hepatocytes, as the lean time control group, showed a flattened cuboidal morphology and native cell-cell contacts, after 7 days of culture (Figure 1B, upper panels). These bright cell-cell contacts on the apical cell surfaces, visible via phase-contrast microscopy, were a good proxy for the bilecanaliculi without the use of any dyes. The median intracellular lipid droplet size (Figure 1B, lower panels) in 7L hepatocytes was 7.48 μ m², and the maximum was 103.90 μm^2 , with a total droplet number of 145 \pm 28 per field (Figure 1C). In 7F hepatocytes (ie, the steatosis group), the lipid droplets increased both in size and number. Specifically, the median lipid size was 13.27 μ m² and the maximum size was 319.10 μ m², while the total number of lipids increased to 1385 ± 253 per field. The 7F hepatocytes showed a loss of visible cell-cell contact in the microscopic images (Figure 1B).

Upon the reversal of steatosis in the reversed 7F7L group, the intracellular lipid droplets in hepatocytes reduced in size, and the median was reduced to 12.44 μm^2 , the maximum was reduced to 269.90 μm^2 , and the total number was decreased to 483 \pm 114 per field (Figure 1*C*). Compared with the 14-day time control, the 14L group, the lipid droplet size in the 7F7L hepatocytes was lower than that of the 14L hepatocytes (median, 10.49 μm^2 ; maximum, 285.70 μm^2), and the number was the same as that in the 14L group (562 \pm 134 per field). Both the 7F7L (reversed) and the 14L (time control) groups displayed brightly visible cell-cell contacts in phase-contrast imaging (Figure 1*B*). Donor-specific data in Figure 1 can be found in detail in Table 1.

We also assessed 2 important hepatic functional markers, albumin and urea, via their measurements in the culture medium of different groups. The urea concentration in the culture medium fluctuated around 55 μ g/mL per day and no difference among the 4 groups, 7L, 7F, 14L, and 7F7L, was observed (Figure 1*D*). The human albumin concentration in the culture medium increased from approximately 15 μ g/mL on day 0 to 60 μ g/mL on day 4, and stabilized thereafter in both 7L and 7F hepatocytes. No difference was seen between the 7F7L and the 14L time control groups (Figure 1*E*).

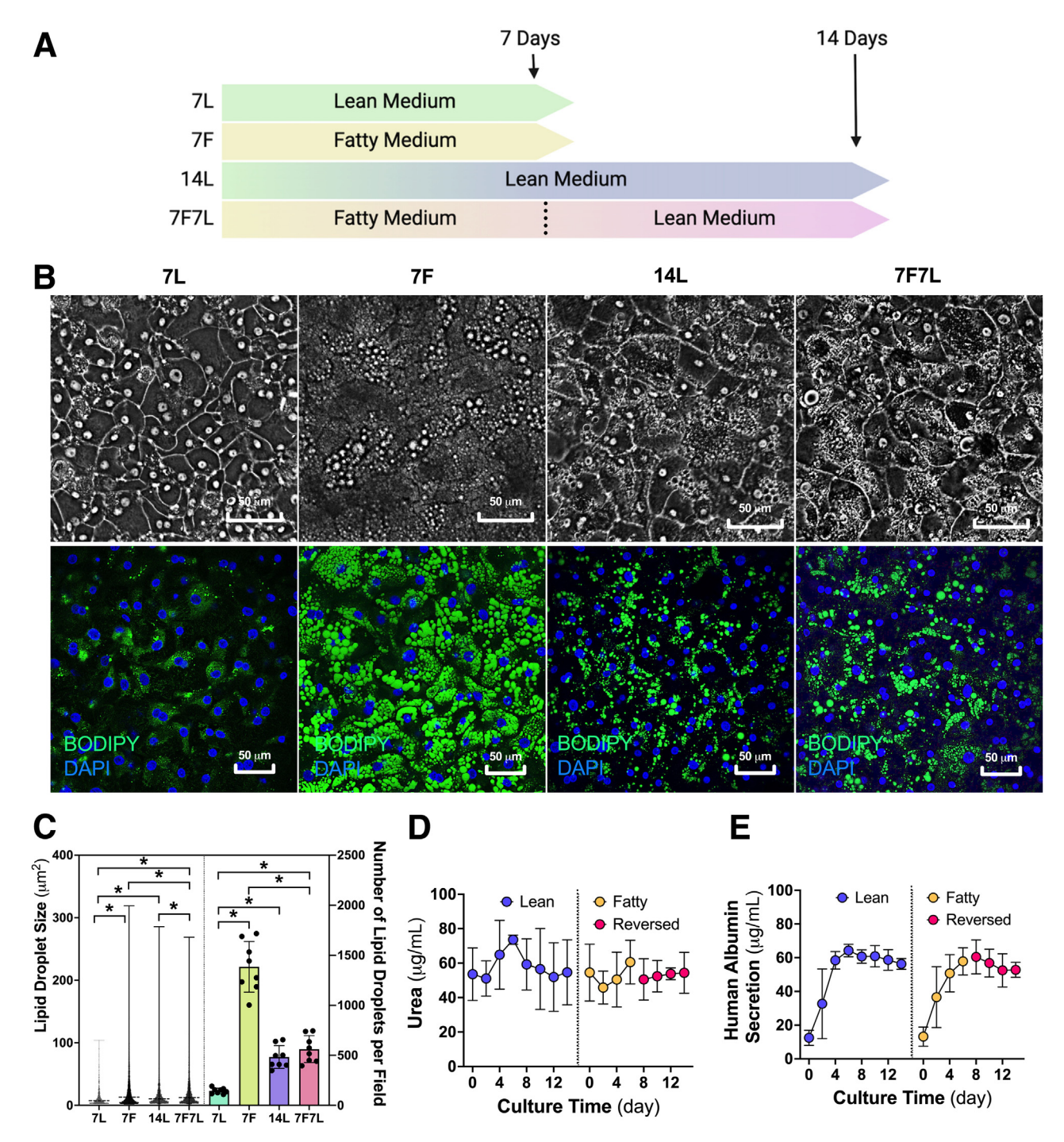


Figure 1. The development and reversal of steatosis in human hepatocytes. (A) The timeline of the development (7F) and reversal (7F7L) of steatosis in human hepatocytes with their corresponding time controls (7L and 14L). (B) Upper panel: Brightfield images of human hepatocytes after the development of steatosis (7F) and after the reversal of steatosis (7F7L) in comparison with their corresponding time controls (7L and 14L). Lower panel: Intracellular lipid droplets stained with BODIPY, and nuclei stained with DAPI in human hepatocytes after the development (7F) and reversal (7F7L) of steatosis in comparison with their time controls (7L and 14L). (C) Quantitation of the size and number of lipid droplets per field in hepatocytes after the completion of the 4 timelines. (D) The time course of the daily urea secreted into the culture medium by hepatocytes in the 4 timelines. (E) The time course of the daily human albumin secreted into the culture medium by hepatocytes. Hepatocyte donors: N = 3. For each donor and each treatment, hepatocytes were cultured in 4–6 separate duplications. For bright-field and fluorescence staining analysis, 6 fields of images were captured in each culture well and subjected to quantitation. Medium from each culture was collected to measure urea and human albumin. Donor-specific data are shown in Table 1. Statistical analyses were performed using a 2-way analysis of variance (ANOVA) followed by the Tukey multiple comparisons test. Data are shown as means ± SD, except for the left panel in panel C, with maximum and minimum values as error bars. *P < .05, 2-way ANOVA, Tukey multiple comparisons.

Table 1.Donor-Specific Data of the Size and Number of Lipid Droplets Developed Within Hepatocytes, Urea, and Albumin Concentration in Culture Medium After Different Treatments

	7L	7F	14L	7F7L	
Size of lipid droplets, μm² Mean					
Donor 1 Donor 2 Donor 3 Maximum	13.03 12.29 12.50	27.57 25.48 26.84	22.86 19.55 15.87	19.29 22.97 26.64	
Donor 1 Donor 2 Donor 3 95th percentile	72.68 90.62 103.94	319.06 269.76 264.76	259.46 285.69 115.83	186.67 258.19 268.88	
Donor 1 Donor 2 Donor 3	39.33 38.44 41.27	95.39 97.63 95.63	89.62 66.21 49.42	65.92 78.07 94.53	
Lipid droplets, n Donor 1 Donor 2 Donor 3	171 ± 19 149 ± 10 117 ± 9	1141 ± 122 1449 ± 270 1469 ± 208	437 ± 55 568 ± 138 418 ± 75	651 ± 135 630 ± 112 429 ± 29	
Urea on day 0, μg/mL Donor 1 Donor 2 Donor 3	74.10 ± 1.49 44.88 ± 0.71 41.69 ± 0.74	75.22 ± 2.22 50.31 ± 5.36 37.98 ± 1.14	N/A N/A N/A	N/A N/A N/A	
Urea on day 7, μg/mL Donor 1 Donor 2 Donor 3	71.86 ± 3.10 75.85 ± 1.71 73.06 ± 1.67	73.07 ± 10.81 61.71 ± 1.15 47.00 ± 3.59	N/A N/A N/A	N/A N/A N/A	
Urea on day 14, μg/mL Donor 1 Donor 2 Donor 3	N/A N/A N/A	N/A N/A N/A	76.42 ± 3.00 35.27 ± 6.69 48.15 ± 5.07	66.04 ± 1.63 40.08 ± 1.90 57.00 ± 1.90	
Albumin on day 0, μg/mL Donor 1 Donor 2 Donor 3	7.68 ± 1.17 16.22 ± 0.84 15.66 ± 1.63	8.89 ± 0.22 19.18 ± 2.96 15.51 ± 8.16	N/A N/A N/A	N/A N/A N/A	
Albumin on day 7, μg/mL Donor 1 Donor 2 Donor 3	62.63 ± 2.76 64.34 ± 5.67 67.84 ± 0.72	63.33 ± 6.74 58.42 ± 2.68 53.04 ± 10.28	N/A N/A N/A	N/A N/A N/A	
Albumin on day 14, µg/mL Donor 1 Donor 2 Donor 3	N/A N/A N/A	N/A N/A N/A	56.49 ± 0.04 58.40 ± 3.47 53.90 ± 2.90	53.71 ± 4.69 51.31 ± 7.02 50.20 ± 5.44	

NOTE. Hepatocytes from 3 donors were each cultured in 4–6 duplicates in different experiments and subjected to the measurement for lipid size and number. The medium was collected for urea and albumin content. Data are shown as means ± SD unless indicated otherwise. Graphical data and statistical analyses are shown in Figure 1.

The Disruption in the F-Actin Cytoskeleton Was Restored After the Reversal of Steatosis, but Not in the Microtubule

We studied the morphology of the F-actin cytoskeleton in all 4 groups using phalloidin staining for the F-actin, and counterstains BODIPY for lipid droplets and DAPI for the nuclei (Figure 2A). We quantitated these results by measuring the number of punctate lumens, stained by phalloidin, in each field (Figure 2B). The F-actin cytoskeleton in the 7L time control was concentrated along the plasma membrane and formed punctate lumens in contact with neighboring cells (7L) (Figure 2A). In contrast, in 7F hepatocytes as the steatosis group, the F-actin network along the plasma membrane was disrupted and the number

of lumens formed by the F-actin was reduced drastically compared with the 7L group (174 \pm 36 vs 323 \pm 28 per field) (Figure 2B). Upon reversal of steatosis, as the reversed 7F7L group, the F-actin cytoskeletal network was restored morphologically and the number of F-actin–positive lumens returned to normal levels (14L, 309 \pm 26 vs 323 \pm 36 per field). These numbers are statistically similar to both the 7L and 14L time controls (323 \pm 28 and 323 \pm 36 per field).

We also assessed the intracellular morphology of the microtubule cytoskeleton by a combination of immunocytochemistry to stain α -tubulin, BODIPY for lipid droplets, and DAPI for nuclei (Figure 2*C*). We quantitated the area covered by α -tubulin in each image field (Figure 2*C*) by measuring its fluorescent signal in the red channel (Figure 2*D*). In 7L

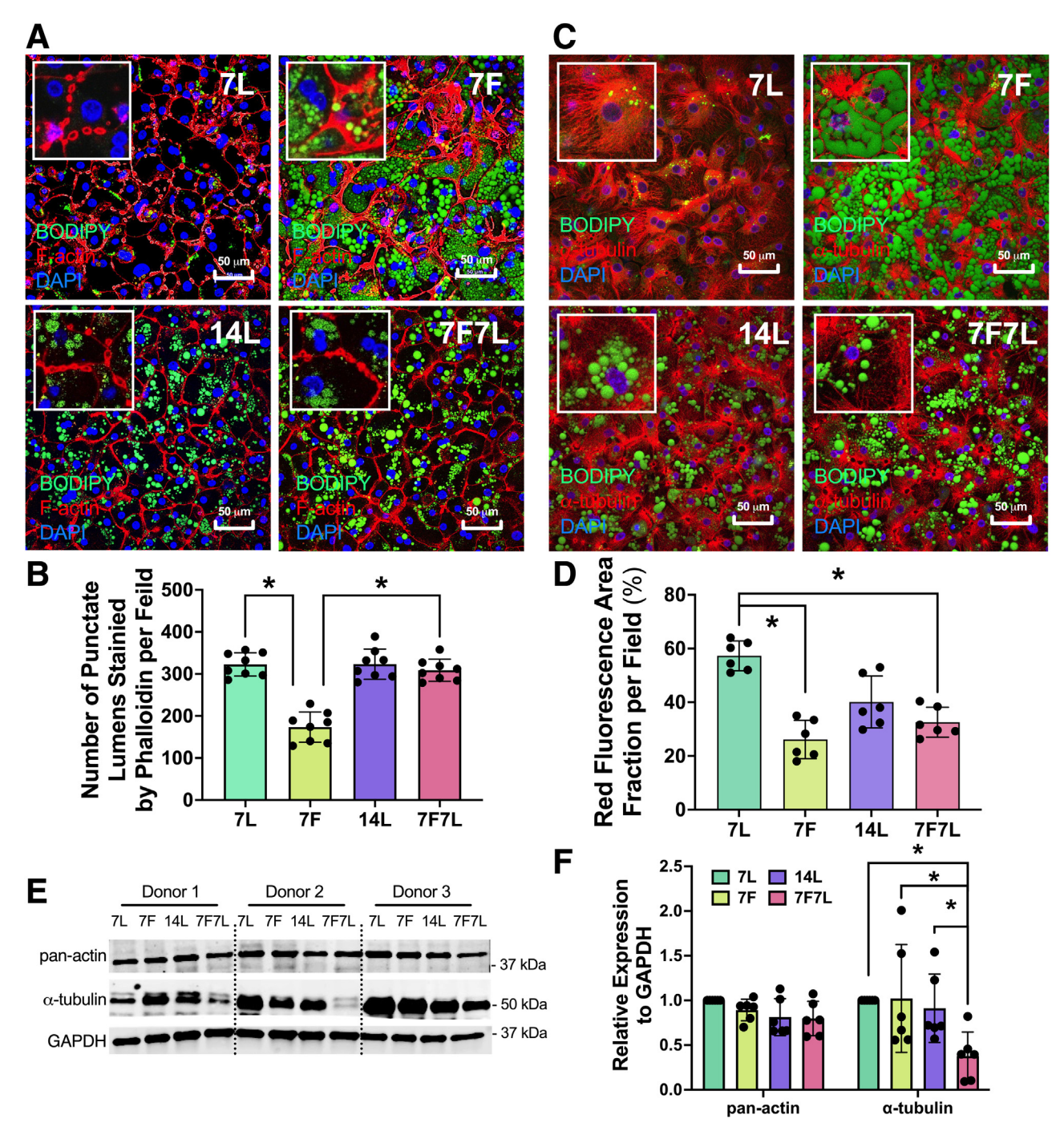


Figure 2. Morphology and protein expression of F-actin and microtubule cytoskeleton in human hepatocytes after the development and reversal of steatosis. (*A*) BODIPY-stained lipid droplets (green), phalloidin-stained F-actin (red), and DAPI-stained nuclei (blue) in human hepatocytes after the development (7F) and reversal (7F7L) of steatosis in comparison with their time controls (7L and 14L). (*B*) Quantitation of punctate lumens along the plasma membrane stained by phalloidin per field in human hepatocytes in the 4 timelines. (*C*) BODIPY-stained lipid droplets (green), immunostained- α -tubulin (red), and DAPI-stained nuclei (blue) in human hepatocytes after the development (7F) and reversal (7F7L) of steatosis in comparison with their time controls (7L and 14L). (*D*) Quantitation of red fluorescent α -tubulin-stained microtubules in the area fraction of each field in human hepatocytes in the 4 timelines. (*E*) Western blots of the expression of the F-actin subunit pan-actin and the microtubule subunit α -tubulin as well as the load control GAPDH. (*F*) Densitometric analyses of the expression of pan-actin and α -tubulin relative to the expression of GAPDH. Expression in all groups for each donor is normalized to the baseline control (7L) from the same donor. Hepatocyte donors: N = 3. For each donor and each treatment, BODIPY and F-actin staining, and BODIPY and α -tubulin were stained separately in 2 and 2–3 duplicated cultures, respectively, and 6 fields of images were captured in each culture and subjected to quantitative analysis. For each donor and each treatment, protein was extracted from 2 separate cultures and subjected to Western blot. Donor-specific data are shown in Table 2. Data are shown as means \pm SD. *P < .05, 2-way analysis of variance, Tukey multiple comparisons.

Table 2.Donor-Specific Data of Morphology Measurement and Protein Expression of F-Actin and α-Tubulin of Hepatocytes After Different Treatments

	7L	7F	14L	7F7L
Punctate lumens sta Donor 1 Donor 2 Donor 3	ained by phalloidin per field, n 321 ± 32 312 ± 32 342 ± 13	186 ± 45 146 ± 24 196 ± 16	303 ± 27 359 ± 28 301 ± 19	304 ± 22 309 ± 43 316 ± 25
Red fluorescence a Donor 1 Donor 2 Donor 3	rea fraction per field, % 63.05 ± 1.34 56.15 ± 5.87 52.70 ± 2.40	34.20 ± 1.13 24.90 ± 4.81 19.30 ± 1.84	33.90 ± 5.80 34.45 ± 2.90 51.95 ± 1.48	29.40 ± 0.28 36.00 ± 6.22 32.35 ± 8.56
Pan-actin expression Donor 1 Donor 2 Donor 3	on to GAPDH 0.73 \pm 0.02 1.10 \pm 0.03 1.24 \pm 0.04	0.72 ± 0.02 1.03 ± 0.03 0.93 ± 0.03	0.78 ± 0.02 0.72 ± 0.02 0.88 ± 0.03	0.74 ± 0.02 0.85 ± 0.02 0.74 ± 0.02
α -tubulin expression Donor 1 Donor 2 Donor 3	n to GAPDH 0.49 ± 0.04 1.12 ± 0.05 1.66 ± 0.08	$\begin{array}{c} 0.75 \pm 0.03 \\ 0.57 \pm 0.03 \\ 1.22 \pm 0.06 \end{array}$	0.62 ± 0.01 0.73 ± 0.04 1.14 ± 0.05	0.27 ± 0.05 0.10 ± 0.01 0.66 ± 0.03

NOTE. Hepatocytes from 3 donors were each cultured in different experiments. Two to 3 duplicated cultures were subjected to BODIPY and F-actin staining, 2 cultures were subjected to BODIPY and α -tubulin, and 2 cultures were subjected to Western blot. Data are shown as means \pm SD. Graphical data and statistical analyses are shown in Figure 2.

hepatocytes, the microtubule was organized as a meshwork of long filaments from the nucleus toward the cell periphery (7L) (Figure 2C), as expected in healthy cells. In 7F hepatocytes, the steatosis group, the microtubule network was disrupted and displaced by lipid droplets, and the microtubules were concentrated along the plasma membrane. Quantitatively, this manifested as a reduction in the intracellular distribution of microtubules in the steatotic hepatocytes (7F) to $26.13\% \pm 7.13\%$ in area fraction per field, compared with the lean time control (7L) of 57.30% \pm 5.53% (Figure 2D). Among the 14L hepatocytes, the microtubules also migrated toward the plasma membrane and formed contiguous channels while maintaining an intracellular microtubular filament distribution of $40.10\% \pm 9.65\%$ in area fraction. Although the intracellular distribution of the microtubule filament in the reversed 7F7L hepatocytes $(32.58\% \pm 5.58\%)$ area fraction per field) was restored to a level higher than 7F, it still was lower than the corresponding 14L time control.

To further elucidate the cytoskeletal changes in our experiments, we studied the change in the expression of cytoskeletal proteins for each study group in each of the 3 human hepatocyte donors. To this end, we used Western blot (Figure 2E) and quantitated the results (Figure 2F). The overall protein expression of pan-actin subunits was not altered in the 7F and 7F7L groups compared with the corresponding time controls of 7L and 14L relative to glyceraldehyde-3-phosphate dehydrogenase (GAPDH) (Figure 2E and F). The protein expression of α -tubulin subunits was not altered in 7F hepatocytes. However, upon the reversal of steatosis, in the 7F7L group, the expression of α -tubulin in hepatocytes was reduced significantly and consistently in all 3 donors. Donor-specific data in Figure 2 can be found in detail in Table 2.

Altered Mitochondrial Dynamics in Human Hepatocytes Recovering From Steatosis

Next, we studied how the intracellular morphology of mitochondria changed after the development and reversal of steatosis. To this end, we used translocase of outer mitochondrial membrane 20 (TOMM20) for immunostaining the mitochondria and a counterstain. DAPI, for nuclei: and characterized the morphology and distribution of mitochondria in the perinuclear area. In 7L hepatocytes, mitochondria were uniformly spherical and distributed around the nucleus (7L) (Figure 3A), taking up $47.27\% \pm$ 13.33% of the 1000- μ m² perinucleus area (Figure 3B). In 7F hepatocytes, the perinucleus distribution of mitochondria was displaced by lipid droplets, leading to a reduction of $27.88\% \pm 12.11\%$ in area fraction in comparison with 7L. In the 14L group, the mitochondria took up $45.23\% \pm 18.93\%$ of the perinucleus area, similar to the 7L hepatocytes. In contrast, the perinuclear mitochondrial distribution in the reversed 7F7L group remained low (32.35% \pm 18.94%) and comparable with the distribution of the steatosis 7F group.

In addition to the differences in the intracellular distribution of mitochondria, we also quantitated the branching and elongation of the mitochondrial network after the development and reversal of steatosis (Figure 3C). For the 2 time-control groups, 7L and 14L, mitochondria showed as spheres in the hepatocytes (7L, 2.48 \pm 0.33 μ m; 14L, 3.26 \pm 0.47 μ m in branch length) (Figure 3C). The spherical morphology was not altered in 7F hepatocytes (3.08 \pm 0.35 μ m, branch length) despite the drastic reduction in the perinuclear distribution as we discussed. In contrast, the elongation of mitochondrial branches increased to 4.58 \pm 0.65 μ m in the reversed 7F7L group, which is significantly higher than both the time controls and steatotic hepatocytes.

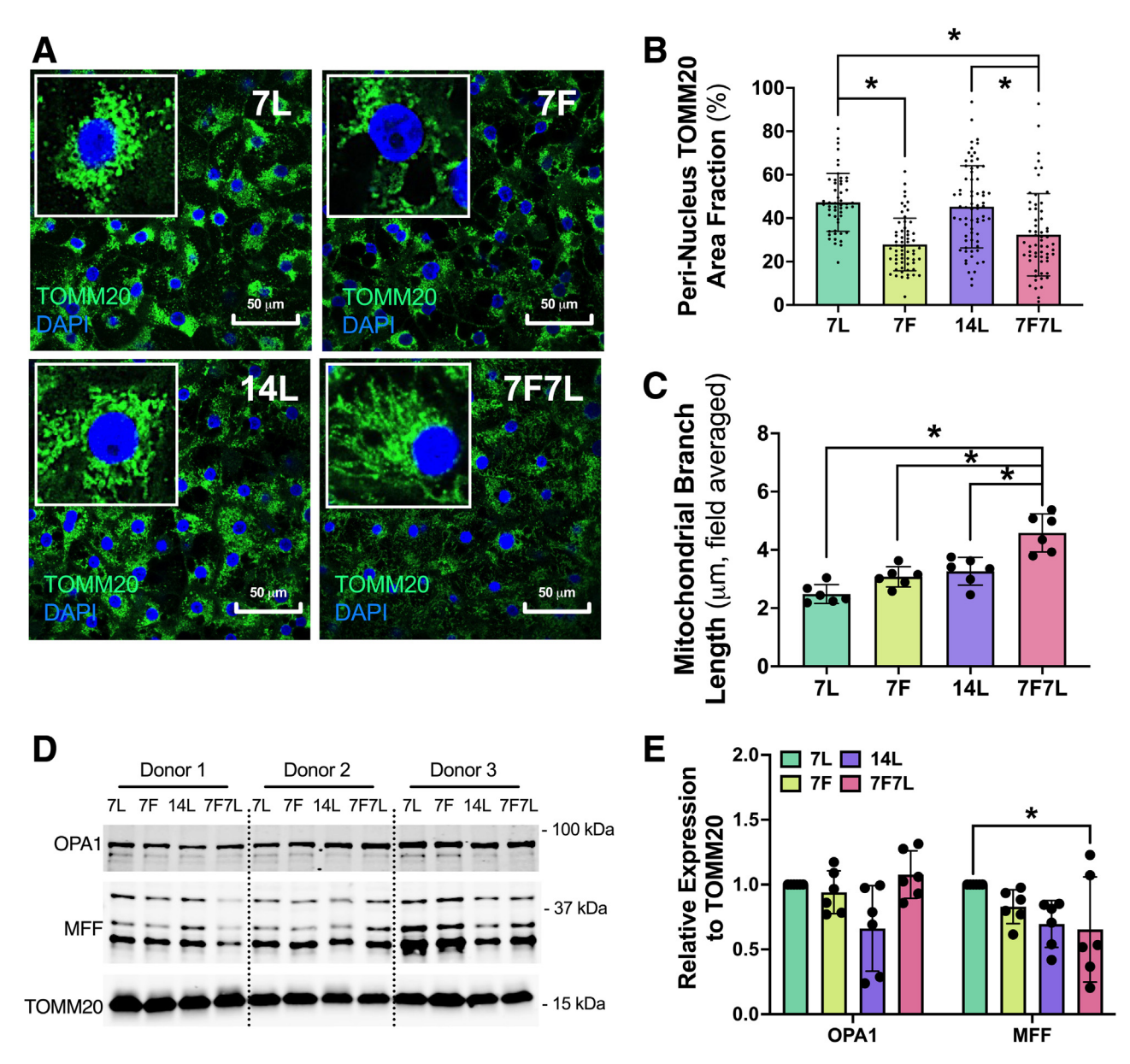


Figure 3. Morphology of mitochondria and expression of mitochondrial dynamic regulatory proteins in human hepatocytes after the development and reversal of steatosis. (A) TOMM20-stained mitochondria (green) and DAPI-stained nuclei (blue) in human hepatocytes after the development (7F) and reversal (7F7L) of steatosis in comparison with their time controls (7L and 14L). (B) Quantitation of green fluorescent TOMM20-stained mitochondria in a fraction of a $1000-\mu\text{m}^2$ perinucleus area in human hepatocytes in the 4 timelines. (C) Quantitation of the length of mitochondria branches in human hepatocytes in the 4 timelines using Fiji: ImageJ plugin MiNA mitochondrial network analysis. (D) Western blots of the expression of the mitochondrial fusion protein OPA1 and fission protein MFF, as well as the mitochondrial load control TOMM20. (E) Densitometric analyses of the expression of OPA1 and MFF relative to the expression of TOMM20. Expression in all groups for each donor is normalized to the baseline control (7L) from the same donor. Hepatocyte donors: N = 3. For each donor and each treatment, hepatocytes were cultured separately in 2 cultures for TOMM20 staining and 6 fields of images were captured from each culture and subjected to analysis. For each donor and each treatment, 2 cultures were prepared for protein extraction and subjected to Western blot analysis. Donor-specific data are shown in Table 3. Data are shown as means \pm SD. *P < .05, 2-way analysis of variance, Tukey multiple comparisons.

We also used Western blots to examine the expression of regulatory proteins for mitochondrial dynamics after the development and reversal of steatosis. Specifically, we assessed the expression of mitochondrial fusion regulatory protein optic atrophy-1 (OPA1), and fission regulatory protein mitochondrial fission factor (MFF) in hepatocytes in

all the study groups individually from 3 donors (Figure 3D and E). There was high heterogeneity in the relative expression of OPA1 in comparison with the mitochondrial housekeeping protein TOMM20 among the 3 donors. Thus, we found no statistically significant difference in the OPA1 expression between the 14L vs 7F7L groups on average

Table 3. Donor-Specific Data of Morphology Measurement of Mitochondrial Dynamics and Associated Mitochondrial Protein Expression of Hepatocytes After Different Treatments

	7L	7F	14L	7F7L
Perinucleus TOMM. Donor 1 Donor 2 Donor 3	20 area fraction, % 42.31 ± 10.11 44.10 ± 14.49 53.46 ± 12.91	26.70 ± 12.88 26.44 ± 13.11 31.21 ± 10.57	38.16 ± 22.98 45.18 ± 15.56 51.48 ± 16.16	38.06 ± 18.29 29.61 ± 12.84 31.72 ± 23.70
Mitochondrial bran Donor 1 Donor 2 Donor 3	ch length, <i>µm</i> 2.74 ± 0.42 2.25 ± 0.10 2.46 ± 0.31	3.32 ± 0.43 2.73 ± 0.22 3.17 ± 0.03	3.52 ± 0.15 3.55 ± 0.28 2.72 ± 0.37	4.07 ± 0.39 5.23 ± 0.21 4.46 ± 0.75
OPA1 expression to Donor 1 Donor 2 Donor 3	TOMM20 1.04 ± 0.15 1.01 ± 0.05 1.28 ± 0.19	1.23 ± 0.11 0.77 ± 0.22 1.22 ± 0.10	0.24 ± 0.57 0.98 ± 0.05 0.94 ± 0.05	0.94 ± 0.11 1.29 ± 0.20 1.31 ± 0.22
MFF expression to Donor 1 Donor 2 Donor 3	TOMM20 0.74 ± 0.15 0.61 ± 0.17 1.49 ± 0.65	0.50 ± 0.98 0.52 ± 0.70 1.29 ± 0.98	0.54 ± 0.18 0.51 ± 0.76 0.68 ± 0.17	0.19 ± 0.40 0.70 ± 1.03 0.77 ± 0.93

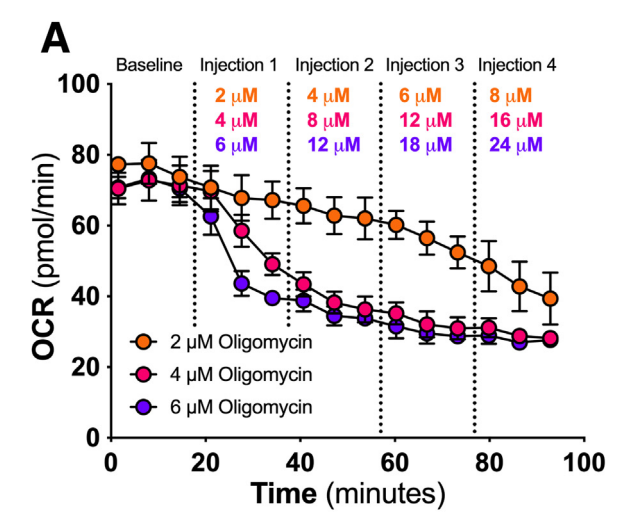
NOTE. Individual donor data for Figure 3. Hepatocytes from 3 donors were each cultured in different experiments. Two duplicated cultures were subjected to TOMM20 staining, and 2 cultures were subjected to Western blot. Data are shown as means \pm SD. Graphical data and statistical analyses are shown in Figure 3.

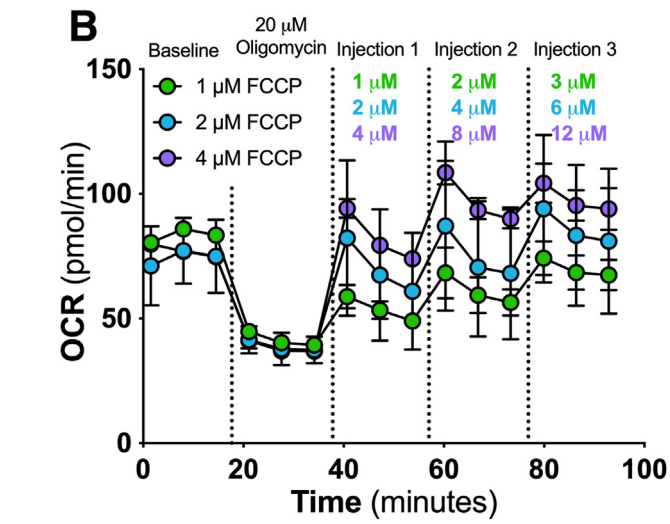
when the results from all donors were pooled, except 7F7L had MFF expression lower than the 7L control when tested under 2-way analysis of variance followed by Tukey multiple comparison (Figure 3E). However, when assessed for each individual donor, the reversed 7F7L hepatocytes had a consistent trend of increasing OPA1 expression (donor 1, 240.9%; donor 2, 31.6%; and donor 3, 41.1%) compared with 14L time controls from the same donors. We also found no statistically significant differences in the overall expression of MFF in the 4 groups when results from all 3 donors were pooled. Donor 1 had a 62.8% reduction in MFF expression in the 7F7L group (circled in Figure 3E) in comparison with the 14L control. On the contrary, donors 2 and 3 had an increased expression compared with the 14L control. This inconsistency also indicated heterogeneity in the expression of MFF when steatosis was reversed. Donorspecific data in Figure 3 can be found in detail in Table 3.

Study of the Mitochondrial Stress and Respiratory Capacity in Human Hepatocytes After the Development and Reversal of Steatosis Titration and dose optimization of oxidative phosphorylation stressors oligomycin, p-trifluoromethoxy-phenylhydrazone, rotenone, and antimycin A in human hepatocytes. We used the Seahorse XF HS mini Analyzer to study the mitochondrial respiration and stress in hepatocytes. In an initial pilot study, we found that the reagent doses recommended by the manufacturer for general cell types were too low to induce any effect in hepatocytes. Specifically, the manufacturer recommended maximum doses of oligomycin, p-trifluoromethoxy-phenylhydrazone (FCCP), and rotenone and antimycin A (Rot/AA) in the Mito Stress Test kit are 2.5, 2, and 0.5 μ mol/L, respectively, (https://www.agilent.com/cs/library/usermanuals/public/ XF_Cell_Mito_Stress_Test_Kit_User_Guide.pdf). Nevertheless,

these doses failed to induce full effects in primary human hepatocytes, likely owing to the substantially higher numbers of mitochondria in hepatocytes compared with most other cell types (Figure 4). Thus, we performed a titration experiment for all 3 drugs in the kit to optimize doses to reach full effects for human hepatocytes. The inhibition of the ATP synthase (complex V) on the electron transport chain by oligomycin reached a plateau phase when the final cumulative concentration increased to more than 18 μ mol/L (Figure 4A). A final concentration of 20 μ mol/L was chosen for oligomycin and used for the evaluation of mitochondrial stress in hepatocytes in the following experiments. The disruption of mitochondrial membrane potential by FCCP reached a plateau phase when the final cumulative concentration increased to more than 8 μ mol/L (Figure 4B). A final concentration of 8 μ mol/L was chosen for FCCP and used for the following evaluation of mitochondrial stress. The inhibition of complexes I and IV in the electron transport chain by Rot/AA reached a plateau phase when the final cumulative concentration increased to more than 3 μ mol/L (Figure 4C). A final concentration of 5 μ mol/L was chosen for Rot/AA and used in the following experiment.

Increased respiration and resistance to ROS in fatty hepatocytes but increased mitochondrial proton leak and susceptibility to ROS when reversed. Using the optimized doses from the earlier titration experiment, we then tested the mitochondrial respiration and stress in hepatocytes after the development and reversal of steatosis using the Seahorse analyzer. We measured the oxygen consumption rate (OCR) after the administration of oligomycin, FCCP, and Rot/AA in steps (Figure 5A). Upon the development of steatosis, the 7F hepatocytes showed increased basal respiration, spared respiratory capacity, ATP production–coupled respiration and maximal respiration in comparison with the 7L time control (Figure 5B). Upon the reversal of steatosis in the





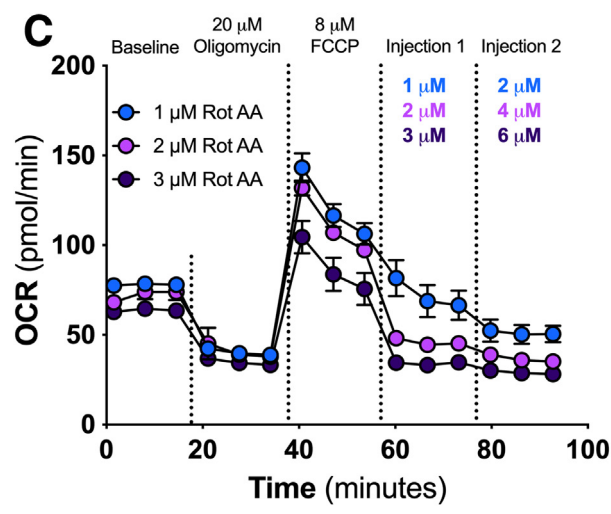


Figure 4. Titration and dose optimization of oligomycin, FCCP, and Rot/AA in human hepatocytes. OXPHOS stressors from the Seahorse XF Cell Mito Stress Kit were subjected to this titration study using a Seahorse XF HS mini Analyzer. (A) The titration of oligomycin was performed by 4-step injections each with a step concentration of 2, 4, and 6 μ mol/L, and reached a final accumulative concentration of 8, 16, and 24 μ mol/L. (B) After an injection of 20 μ mol/L

7F7L hepatocytes, the basal respiration and ATP production–coupled respiration levels returned to the time control levels, while both the spare respiratory capacity and maximum respiration remained increased compared with the 14L time control. Furthermore, an increased proton leak was observed only in the reversed 7F7L hepatocytes.

We then measured the response of hepatocytes to H_2O_2 exposure to assess their susceptibility to ROS-induced cell death during the development and reversal of steatosis. Specifically, hepatocytes in the 4 study groups were treated with a wide range (50, 100, 500, 1000, 5000, 10,000, and 50,000 μ mol/L) of H_2O_2 upon the completion of their respective timelines. We then measured the viability of hepatocytes in this dose-response study via the 3-(4,5dimethylthiazol-2-yl)-2,5-diphenyltetrazolium assay for all 4 groups (Figure 5C). Among the 2 time-control groups, 7L hepatocytes had an H2O2 median inhibitory concentration (IC₅₀) of 1290.50 \pm 987.51 μ mol/L while the 14L hepatocytes had an H_2O_2 IC₅₀ of 1023.93 \pm 434.36 μ mol/L (Figure 5D). In comparison, the 7F hepatocytes became more resistant to ROS with an increased H₂O₂ IC₅₀ of 3182.67 + 787.11 μ mol/L. However, in the reversed 7F7L group, hepatocytes became more susceptible to ROSinduced damage, and the H2O2 IC50 was reduced to $462.53 \pm 117.46 \ \mu mol/L$. Donor-specific data in Figure 5 can be found in detail in Table 4.

Discussion

To better resemble the in vivo environment, the in vitro culture of hepatocytes was performed in a "sandwich" configuration, in which cells were cultured on a single surface and overlaid with a second layer of extracellular matrix (ECM), 48 this configuration resembles the thickness and structure of a hepatic plate, which is usually 1-2 cells thick.⁴⁹ The ECM substrate typically consists of type I collagen,⁵⁰ or a soluble form of basement membrane purified from Engelbreth-Holm-Swarm tumor cells, 51,52 such as Matrigel (Corning Inc.) and Geltrex (Thermofisher Scientific). The sandwich configuration induces increased activities of liver-specific functions and expression of liver-specific markers compared with cultures on a single surface of ECM. 50,53 In particular, the sandwich-cultured hepatocytes mimic the organization and expression of cytoskeletal proteins that are found in the liver.54

In sandwich-cultured hepatocytes, the cytoskeleton network initially forms bile canaliculi as punctate lumina

oligomycin, the titration of FCCP was performed by 3-step injections each with a step concentration of 1, 2, and 4 μ mol/L, and reached a final accumulative concentration of 3, 6, and 12 μ mol/L. (C) After an injection of 20 μ mol/L oligomycin and 8 μ mol/L FCCP, the titration of Rot/AA was performed by 2-step injections each with a step concentration of 1, 2, and 3 μ mol/L, and reached a final accumulative concentration of 2, 4, and 6 μ mol/L. The detailed procedure of the titration and dose optimization of all 3 drugs are shown in Table 2. Titration experiments were conducted using hepatocytes from donor 1 and each concentration was repeated in 3 duplications.

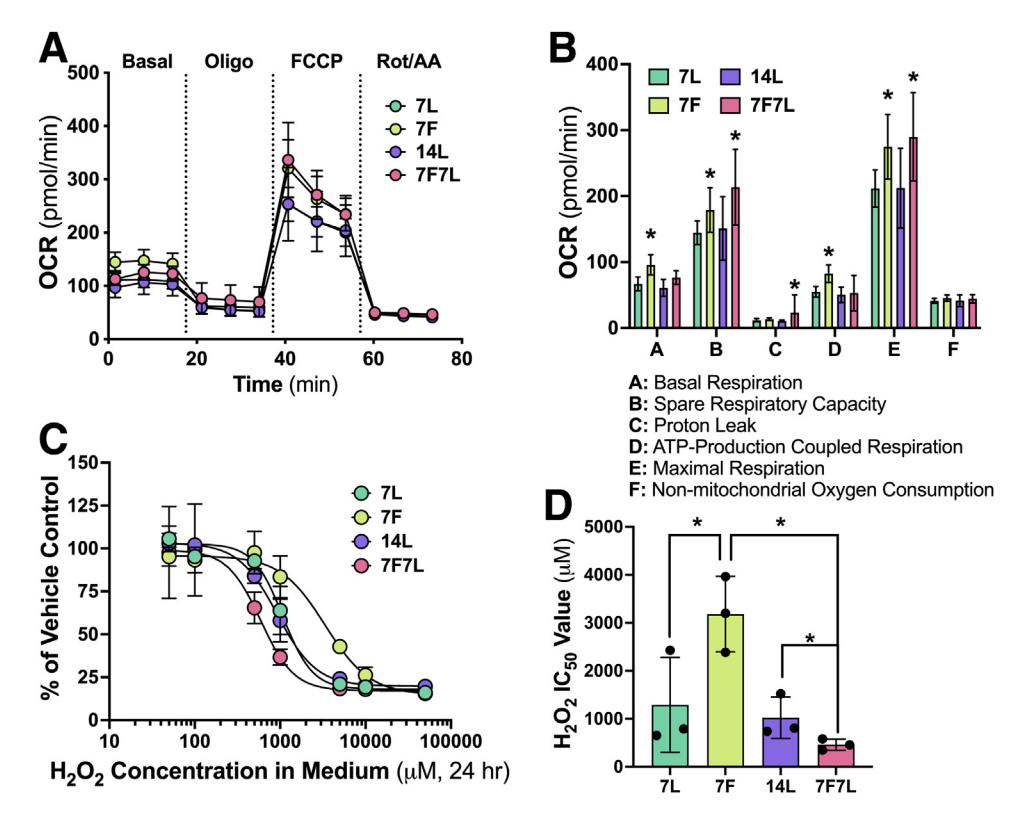


Figure 5. Evaluation of mitochondrial functions and respiration, and viability dose response of H_2O_2 in human hepatocytes after the development and reversal of steatosis. (A) The time course of OCR in the execution of Seahorse XF Cell Mito Stress Kit protocol using a Seahorse XF HS mini analyzer. (B) Analyzed data from the OCR time course in panel A showing the mitochondrial basal respiration, spared respiratory capacity, proton leak, ATP production–coupled respiration, maximal respiration, and nonmitochondrial oxygen consumption in human hepatocytes after the development (7F) and reversal (7F7L) of steatosis in comparison with their time controls (7L and 4L). (C) Cell viability was measured using a 3-(4,5-dimethylthiazol-2-yl)-2,5-diphenyltetrazolium bromide assay of human hepatocytes after the completion of the 4 timelines and treated with a range of H_2O_2 for 24 hours. Values were normalized to the level of vehicle controls. (D) The IC_{50} of IC_{50}

between cell borders and later forms into a contiguous anastomosing network. However, when cultured without an overlay, canalicular formation varies in rate and extent and disappears as hepatocytes detach and die in 5-7 days after plating. 52,55 In practice, the top layer of ECM presents a barrier for hepatocytes to exchange nutrients and signal molecules and exosomes with the bulk of the culture medium.⁴⁸ This can be a major challenge when creating pharmacologically induced models in which drugs and substrates are administered to hepatocytes, and when studying the content within secreted exosomes from sandwich-cultured hepatocytes because the top layer likely interferes with the diffusion of exosomes. Thus, in this study, we used a method in which a daily 2% Geltrex supplementation to the culture medium allowed the hepatocytes to immobilize the soluble ECM substrate freely without an excessive thick top coating. This free coating method allowed hepatocytes to be stably cultured for 2 weeks with consistent production of urea and albumin, 2 prototypical functional markers of hepatocyte function (Figure 1D and E). We note that, beyond these 2 markers, the fatty medium might alter transcriptomic profiles

of the culture hepatocytes and subsequent metabolic activity, including drug metabolic activity as we recently have shown. Hepatocytes subjected to the free coating method also showed an in vivo-like organization of the cytoskeleton, as seen in Figure 2A and C, which was similar to that described in the previous sandwich-cultured hepatocytes. 48,54,55

Disruptions in the cytoskeletal network have been found in the altered hepatocyte functions in alcohol-induced liver disease. The F-actin filament is vital in maintaining the polarization of the cell and regulating vesicle dynamics and trafficking. The cell and regulating vesicle dynamics and trafficking. Acetaldehyde, which is an ethanol metabolite, covalently modifies the F-actin filament and impairs actin-regulated attachment between hepatocytes and ECM. Meanwhile, the microtubule as a central component of cellular dynamics including organelle distribution, mitosis, and vesicle/exosome motility, also is modified covalently by the acetaldehyde and shows an impaired polymerization. This disruption in cytoskeletons sabotages the trafficking of hepatic proteins and destabilizes hepatocyte attachment to ECM.

Table 4. Donor-Specific Data of Seahorse Analyses Evaluating Mitochondrial Function and Respiration, and IC₅₀ of H₂O₂ Stress Test in Hepatocytes After Different Treatments

	7L	7F	14L	7F7L
Basal respiration Donor 1 Donor 2 Donor 3	66.93 ± 7.65 69.68 ± 6.32 64.73 ± 8.64	100.10 ± 16.26 91.96 ± 13.68 91.423 ± 17.97	58.76 ± 6.16 62.77 ± 8.28 56.96 ± 15.41	73.79 ± 3.26 77.72 ± 3.76 70.06 ± 16.86
Spare respiration of Donor 1 Donor 2 Donor 3	capacity 131.39 ± 13.78 135.58 ± 16.04 158.36 ± 23.71	188.78 ± 42.25 151.48 ± 30.36 181.55 ± 53.97	138.74 ± 52.23 125.23 ± 31.56 163.00 ± 30.37	189.17 ± 52.77 203.99 ± 75.66 250.90 ± 48.41
Proton leak Donor 1 Donor 2 Donor 3	12.32 ± 0.29 12.00 ± 0.33 15.86 ± 0.57	11.74 ± 1.50 13.99 ± 1.83 14.72 ± 1.88	10.74 ± 1.27 10.31 ± 0.89 11.60 ± 0.49	58.45 ± 24.73 28.02 ± 11.92 16.34 ± 63.20
ATP production—co Donor 1 Donor 2 Donor 3	cupled respiration 59.54 ± 10.23 60.32 ± 5.64 62.47 ± 7.54	86.62 ± 19.39 79.92 ± 11.92 83.12 ± 22.09	44.05 ± 6.37 53.30 ± 17.91 49.76 ± 6.49	54.45 ± 26.92 71.74 ± 12.97 40.32 ± 31.62
Maximal respiration Donor 1 Donor 2 Donor 3	216.35 ± 36.57 209.51 ± 25.26 190.67 ± 7.67	261.47 ± 40.17 255.92 ± 32.04 309.50 ± 43.42	235.6 ± 24.14 214.78 ± 70.02 188.96 ± 75.34	333.66 ± 92.78 300.53 ± 71.63 206.89 ± 124.44
Nonmitochondrial of Donor 1 Donor 2 Donor 3	oxygen consumption 40.26 ± 6.37 34.86 ± 3.32 38.96 ± 0.99	45.71 ± 4.94 47.75 ± 5.30 45.53 ± 2.21	43.84 ± 8.35 33.62 ± 12.02 44.58 ± 6.08	36.24 ± 1.69 46.87 ± 11.90 38.75 ± 6.62
H ₂ O ₂ IC ₅₀ value, μ. Donor 1 Donor 2 Donor 3	mol/L 791 2428 653	3962 2388 3198	740 807 1524	583 348 457

NOTE. Individual donor data for Figure 5. Hepatocytes from 3 donors were each cultured in different experiments. Three duplicate cultures were subjected to Seahorse experiments, and $3 H_2O_2$ assays were formed for each of the timelines. Data are shown as means \pm SD. Graphical data and statistical analyses are shown in Figure 5.

Although the role of cytoskeletons in the development of alcohol-induced liver disease has been well elucidated, to our knowledge, the alteration of cytoskeletal dynamics in the development and reversal of NAFLD remained unclear. In this study, we showed that the accumulation of lipid droplets displaced and disrupted the cytoskeleton network in hepatocytes after the development of steatosis. Although the pathologic mechanism of cytoskeletal disruption is different from the ethanol-induced acetaldehyde adduction in alcohol-induced liver disease, such an impairment may induce similar downstream effects in hepatocytes such as organelle or vesicle trafficking.

To explore one of the downstream effects of cytoskeleton disruption, we evaluated the mitochondrial dynamics and function in fatty hepatocytes. Mitochondrial dynamics are highly dependent on their interactions with the microtubule and F-actin cytoskeleton. Mitochondria are translocated actively in the cell along the microtubule as an adaptive mechanism in response to changes in energy and metabolism landscape in the cell.^{29,31,42} Although the microtubule regulates long-range movements of mitochondria, F-actin coordinates short-range motility of mitochondria,³⁶ anchoring in high-energy-demanding sites,³⁷ and dynamics of fusion/fission.³⁹⁻⁴¹

In this study, the microtubule and F-actin cytoskeletons in hepatocytes were displaced by lipid droplets after the development of steatosis (7F) (Figure 2A and C). This displacement in cytoskeletons overlapped with an altered distribution of mitochondria (7F) (Figure 3A). After a 7-day culture in the fatty medium, no prompt changes were seen in mitochondrial dynamics regarding morphology (7F) (Figure 3A) and expression of OPA1 and MFF (Figure 3D) and E). However, increases in basal mitochondrial respiration, spare respiration capacity, and maximum respiration were observed in the 7F hepatocytes (Figure 5B). This increment indicated an adaptation of mitochondrial function to higher metabolic demand during excessive lipid accumulation. This adaptation also manifested itself as an increased resistance to ROS-induced stress and promoted the survival of hepatocytes treated with H₂O₂ (Figure 5C and D). This observation is in line with reports on the increase of fatty acid oxidation and respiratory functions in mitochondria from human biopsy specimens, 18,19,69 and in vivo models at early stages of NAFLD, 70,71 such as steatosis and the onset of NASH. The acquired ability of mitochondria sustains a hyperactivated metabolic activity that promotes ROS production, which is a key mechanism that contributes to a subsequent defect in lipid metabolism, activation of mitophagy, and inflammatory pathway in the transition to late-stage NAFLD. 18,72

A part of our team previously showed an increased sensitivity to hypoxia/reoxygenation stress in hepatocytes after reversal from steatosis, in comparison with a lean culture. The reversal from steatosis improved the ATP production and glutathione disulfide/reduced glutathione ratio compared with their impaired condition in steatotic hepatocytes. Still, neither ATP production nor the glutathione disulfide/reduced glutathione ratio recovered to the levels in the lean control. 26,73 The underlying mechanism of this insufficient recovery was unclear. In the current study, we observed that the expression level of α -tubulin was reduced in a consistent manner among all 3 donors of hepatocytes upon reversal of steatosis (7F7L) (Figure 2E and F). This variation in the expression level of α -tubulin indicates α -tubulin may not be an ideal housekeeping protein for use in Western blots with samples related to fatty livers. We note that the distribution of α -tubulin (Figure 2D) and the protein expression levels (Figure 2F) are not correlated in terms of the group-wise comparisons. This is because the distribution (ie, area coverage) is highly affected by the crowding from accumulating lipids whereas the expression levels need not be affected by such crowding. This was well observed by the fact that the 7F7L group has a higher α tubulin area fraction, upon the removal of crowding lipids, than the 7F group (Figure 2D), despite a much lower expression (Figure 2F). Notably, the 7F7L group shows a lower intensity than 7F in α -tubulin (Figure 2C), which correlate well with the expression levels as expected because staining intensity is a proxy measure for expression levels. Nevertheless, quantification and comparisons based on intensity were technically prohibitive, hence Western blot was conducted as a reliable and quantitative measure of protein expression levels.

The reduction in microtubule expression was associated with increased mitochondrial branch length (7F7L) (Figure 3A and C), indicating that mitochondrial fusion is predominant in hepatocytes upon reversal of steatosis. The mitochondrial fusion marker OPA1 was increased in hepatocytes upon reversal of steatosis compared with their time controls when we examined each hepatocyte donor individually (Figure 3E). However, because of high donor heterogeneity of the relative expression of OPA1 normalized by TOMM20, the difference in OPA1 expression between the 14L and 7F7L groups failed to produce significance when results from different donors were pooled. Similar heterogeneity was noted as we studied the expression level of MFF, however, we did find significant reduction of MFF expression in reversed 7F7L hepatocytes compared with the 7L control group, indicating reduced fission capability. The altered mitochondrial morphology (ie, increased branch length) was correlated with increased mitochondrial proton leak (Figure 5B) and susceptibility to ROS-induced damage in reversed 7F7L hepatocytes (Figure 5C and D). An increased ROS level and susceptibility to ROS-induced damage also were observed in NAFLD/NASH patients, 74,75 which also was attributed to an impairment in mitochondrial respiratory capacity and exacerbated proton leak. 18,76

In addition, we performed a dose optimization study of OXPHOS stressors (oligomycin, FCCP, and Rot/AA) in primary human hepatocytes. The mitochondrial bioenergetic profile and resistance to OXPHOS stressors are distinct in various cell types, such as leukocytes,⁷⁷ HepaRG,⁷⁸ and cell lines.⁷⁹⁻⁸¹ The effective doses can differ significantly from those recommended by the manufacturer of mitochondrial stress tests. In this aspect, our optimized results showed that substantially higher doses of the OXPHOS stressors are required to achieve the full effect of such stressors in primary human hepatocytes. We posit that this is likely owing to the high mitochondria content in hepatocytes (2000-4000 per cell),82,83 in comparison with some other energy-intensive cells such as macrophages up to 700 mitochondria per cell and skeletal muscle cells 140 per cell.⁸⁴ We hope that the optimized doses for the OXPHOS stressors, commonly used in metabolic analyses on the Seahorse platforms (Agilent Technology, Cedar Creek, TX) and others, may serve as a reference for the scientific community who are studying mitochondrial function in primary human hepatocytes. We are not aware of any previously published dose optimization in primary human hepatocytes.

There were several limitations to this reported study. First, the results presented are from 3 human biological donors, and thus are primarily representative of these donors. To generalize to all human hepatocytes (ie, the general population) a larger cohort study is in order. Still, we posit that this small cohort can serve as a pilot study, not to answer a particular question but to put forth the right question to ask for further large cohort and in vivo studies.

The short time course for in vitro experiments is another limitation in which we maintained human primary hepatocyte cultures for only 2 weeks whereas NAFLD in human beings takes months to years to develop. Still, our model shows that the damage resulting from lipid accumulation (steatosis) can be observed in an accelerated time frame, 1 week, in vitro compared with the time it takes for a liver to reach a similar level of injury. We thus posit that our simple in vitro model serves as a good framework to study mitochondrial damage resulting from steatosis and its reversal by the withdrawal of the same conditions within the same time frame (1 week). In this regard, we note that the hepatic mitochondria have a considerably faster turnover half-life (2-4 days) in comparison with many other tissues in vivo with mitochondrial half-lives on the order of weeks.^{85,86} Despite multiple turnover cycles—2 or more within 1 week—for mitochondria to be recovered, we still observed several persistent changes in mitochondrial dynamics during the time frame of our studies. Nevertheless, we cannot conclude that the mitochondria function or morphology, after the reversal of steatosis, will not further ameliorate or exacerbate beyond the time course of our in vitro study. Furthermore, we note that our results also might indicate that the cytoskeletal disruption, especially in the microtubule network, might have delayed or impaired the mitochondrial turnover process (ie, mitochondrial biogenesis). This interpretation is supported by the significant involvement of microtubules in the fusion and fission processes that drive the mitochondrial biogenesis. 87,88

Despite the limitations, this study showed a mechanism of hepatocyte injury during their recovery from steatosis, which is owing to cytoskeleton and mitochondrial impairment associated with hyperactive lipid metabolism and ROS. Whether such impairment exists and also persists in NAFLD patients as their liver recovers requires in vivo animal and human studies. Indeed, follow-up in vivo studies to investigate the level at which simple steatosis results in irreversible changes and impair full recovery is in order and will be performed in the future.

Overall, we developed a long-term culture method of human hepatocytes to maintain in vivo-like cytoskeleton and metabolism characteristics and used this model in generating an in vitro steatosis model to study the alteration of cytoskeletal and mitochondrial dynamics in the development and reversal of steatosis. We found that in 7 days after the induction of steatosis, the formation of bile canaliculi by F-actin was disrupted and the intracellular microtubule network was displaced by lipid droplets. This change in cytoskeletal morphology upon steatosis was accompanied by mitochondrial adaptations indicated by increased basal and maximum capacity of respiration, and resistance to H₂O₂-induced cell damage. These initial adaptive responses to oxidative insults in the early phases of lipid accumulation also have been reported by others.⁸⁹⁻⁹¹ After a 7-day reversal of steatosis by withdrawing the FFA supplement, the F-actin formation of bile canaliculi was restored, but there was a reduction in the protein expression of the microtubule subunit α -tubulin. This reduction of microtubule was accompanied by elongation of mitochondrial branches, exacerbated proton leaks across the mitochondrial membrane, and increased susceptibility to H₂O₂induced cell death. Our study showed that the alterations in cytoskeleton and adaptation of mitochondria are among the underlying mechanisms in the pathology and changed hepatic functions in NAFLD. However, most importantly, such changes can persist and continuously contribute to the predisposition of liver tissue to oxidative stress and liver injury even when steatosis morphology is reversed morphologically by gross measures. In future studies, we will further investigate the downstream effect of cytoskeletal and mitochondrial impairment in hepatocytes under steatosis and reversed steatosis, especially regarding the transportation and metabolism of xenobiotics that are highly dependent on a functional cytoskeletal and mitochondrial network.

Materials and Methods

Primary Human Hepatocyte Culture

Primary human hepatocytes were purchased from the Cell Resource Core of the Massachusetts General Hospital. Hepatocytes were isolated from livers after the cardiac death of 3 donors and cryopreserved. Donor information including gender, age, body mass index, cause of death, and warm ischemia time after cardiac death were provided by the Cell Resource Core and are shown in Table 5. Cryopreserved hepatocytes were thawed in a 37°C water bath and recovered in 45% Percoll density gradient medium (17089109; Cytiva,

Table 5.Donor Information of Human Hepatocytes Used in the Study

	Donor 1	Donor 2	Donor 3	
Gender	Male	Male	Female	
Age, y	36	52	47	
Body mass index	38.4	27.6	46.9	
Cause of death	Head trauma	Anoxia	Anoxia	
Warm ischemia time after cardiac death, <i>min</i>	19	29	17	

Marlborough, MA) in Dulbecco's modified Eagle medium, followed by centrifugation at $100 \times g$ for 10 minutes. Pellets were resuspended in William's Medium E supplied with 10% fetal bovine serum, 0.5 U/mL insulin, 7 ng/mL glucagon, 20 ng/mL epidermal growth factor, 7.5 ug/mL hydrocortisone, 200 U/mL penicillin, and 200 μ g/mL streptomycin. Hepatocytes were seeded into 12-, 24-, or 96-well plates precoated with 1% Geltrex (A1413202; Thermo Fisher Scientific, Waltham, MA) at densities of 800,000, 400,000, or 40,000 cells per well, respectively. Allowing 40 minutes for the hepatocytes to attach, the medium was replaced with hepatocyte basal medium (CC3199; Lonza, Portsmouth, NH) supplemented with hepatocyte growth factor supplement (CC4182; Lonza) and 2% Geltrex. In 24 hours, the hepatocytes were ready and subjected to 4 different experimental timelines as described later.

Steatosis Induction and Reversal

The timelines of induction and reversal of steatosis in human hepatocytes are shown in Figure 1A. The lean medium was formulated using the hepatocyte basal medium (Lonza) supplied with hepatocyte growth factors (Lonza) and the corresponding volume of the dimethyl sulfoxide vehicle. Hepatocytes cultured in the lean medium (without FFA) were assigned as 7L and 14L, corresponding to culture time. Steatosis was induced by culturing hepatocytes in a fatty medium, which was based on the lean medium with a supplement of 800 μmol/L oleic acid (unsaturated fatty acid, 01383; Sigma-Aldrich), and 400 μmol/L palmitic acid (saturated fatty acid, F0500; Sigma-Aldrich) that were predissolved in dimethyl sulfoxide. Hepatocytes treated with the fatty medium for 7 days were assigned as 7F groups in the 7L group. To reverse steatosis, the culture medium was switched to the lean medium for another 7 days after the completion of the treatment of 7 days of the fatty medium, and thus assigned as the 7F7L group and subjected to comparison with the 14L group. Both the lean and fatty medium were supplied with 2% Geltrex.

Measurement of Urea and Albumin Concentrations in the Culture Medium

The culture medium was collected daily and subjected to the measurement of urea and albumin concentration. The measurement of urea was conducted using a colorimetric diacetyl monoxime assay (157421; Stanbio Laboratories, Boerne, TX), the assay was prepared in accord with the

Table 6. Experiment Design for Titration and Dose Optimization of Oligomycin, FCCP, and Rot/AA in Human Hepatocytes to Evaluate Mitochondrial Functions and Respiration

	Step concentration		Injection port loading			
Drug	(10×)	A, 20 μL	B, 22 μL	C, 25 μL	D, 27 μL	Final concentration
Oligomycin	20 μmol/L 40 μmol/L 60 μmol/L	+ + +	+ + +	+ + +	+ + +	$2+2+2+2=8 \mu \text{mol/L} \ 4+4+4+4=16 \mu \text{mol/L} \ 6+6+6+6=24 \mu \text{mol/L}$
FCCP	10 μmol/L 20 μmol/L 40 μmol/L	200 μ mol/L Oligo (10 \times) ^a 200 μ mol/L Oligo (10 \times) ^a 200 μ mol/L Oligo (10 \times)	+ + +	+ + +	+ + +	$1+1+1=3~\mu mol/L \ 2+2+2=6~\mu mol/L \ 4+4+4=12~\mu mol/L$
Rot/AA	10 μmol/L 20 μmol/L 30 μmol/L	200 μ mol/L Oligo (10 \times) ^a 200 μ mol/L Oligo (10 \times) ^a 200 μ mol/L Oligo (10 \times) ^a	80 μ mol/L FCCP (10 \times) ^a 80 μ mol/L FCCP (10 \times) ^a 80 μ mol/L FCCP (10 \times) ^a	+ + +	+ + +	$1 + 1 = 2 \mu \text{mol/L}$ $2 + 2 = 4 \mu \text{mol/L}$ $3 + 3 = 6 \mu \text{mol/L}$

NOTE. In the Step concentration column, the number indicates the concentration of 10× stock solution that loaded to the injection port. In the Final concentration column, the number indicates the concentration of the drug in the well after the drug was injected from the port into the well, and cumulatively as steps of injections occurred.

^aOptimized dose based on the titration result before the testing of the subject drug.

manufacturer's protocol, and the measurement was performed using a plate reader by reading absorbance at 520 nm. The human albumin content in the medium was measured using a Human Albumin Enzyme-Linked Immunosorbent Assay kit (EHALBX5; Thermo Fisher Scientific). The culture medium was diluted 1000 times using the assay diluent to be within the range of the standard curve and the assay was prepared according to the manufacturer's instructions, and the measurement was performed using a plate reader by reading absorbance at 450 nm.

Staining of Lipid, Cytoskeleton, and Mitochondria in Immunocytochemistry

Hepatocytes were washed with phosphate-buffered saline, incubated with BODIPY (2 µmol/L, D3922; Thermo Fisher Scientific) at 37°C for 15 minutes, then processed for further fixation and staining. Hepatocytes were washed with phosphate-buffered saline and fixed using 4% formaldehyde solution (WC324416; Thermo Fisher Scientific), permeabilized using 0.25% Triton X-100 (SLCC5539; Sigma-Aldrich, St. Louis, MO), and incubated with 1% bovine serum albumin to block unspecific staining. Subsequently, hepatocytes were incubated with Phalloidins (1:400, A12381; Thermo Fisher Scientific) to stain F-actins, primary antibodies targeting α -tubulin (1:500, ab190573; Abcam, Cambridge, MA), or TOMM20 targeting mitochondria (1:500, ab283317; Abcam). After washing with phosphate-buffered saline, hepatocytes were incubated with corresponding secondary antibodies with Alexa Flour 594 or 647 fluorescence (Abcam) and mounted in an antifade mountant with DAPI (P36931; Thermo Scientific). Images were captured using a Nikon A1R confocal microscope (Nikon, Melville, NY).

Image Quantitation

Images were converted to 8-bit RGB (red, green and blue) images and quantitated using NIS-Element D4.6 software (Nikon). To determine the number and size of lipid droplets in hepatocytes, objects in the green channel were

thresholded for intensity (low, 20; high, 255) and circularity (low, 0.2; high, 1). The selected patterns were measured for their size in μm^2 and counted for number per field. The number of F-actin-stained bile canaliculi was determined by thresholding for intensity (low, 55; high, 255) and size of patterns (low diameter, 1 μ m; high, 10 μ m) in the red channel; the quantitation is presented as the number of Factin-positive bile canaliculi per field. To quantitate the formation of microtubules and the distribution of mitochondria, patterns were thresholded for intensity (microtubule: low, 30; high, 255; mitochondria: low, 20; high, 255). The fluorescent area was measured as the selected area fraction of the whole field to quantitate microtubule density or within the $1000-\mu m^2$ area of a nucleus to quantitate the perinucleus distribution of mitochondria. The mitochondrial branch length was measured using Fiji: ImageJ (National Institutes of Health) plugin MiNA - Mitochondrial Network Analysis (https://imagej.net/plugins/mina).

Western Blot

Hepatocytes were lysed using TRI reagent (T9424; Millipore Sigma, Burlington, MA). After centrifugation at 9000 \times g for 15 minutes at 4°C, the supernatant was collected and samples were normalized for protein concentration. The proteins were electrophoresed on an sodium dodecyl sulfate-polyacrylamide gel, and then transferred to a nitrocellulose membrane using a Trans-Blot Turbo Transfer System (Bio-Rad, Hercules, CA). The membrane was blocked with 3% skim milk and then incubated with primary antibodies against pan-actin (1:500, ab1801; Abcam), α -tubulin (1:1000, ab52866; Abcam), OPA1 (1:500, ab157457; Abcam), MFF (1:4000, 17090-1-AP; Thermo Scientific), TOMM20 (1:4000, ab186735; Abcam), and GAPDH (1:4000, ab9485; Abcam). The membrane was probed with IRDye 800CW or IRDye 680RD secondary antibodies (LI-COR Biotechnology, Lincoln, NE), and then imaged and analyzed with the Odyssey DLx imaging system (LI-COR Biotechnology). The relative expression to GAPDH

or TOMM20 was calculated for each protein and normalized to the value of control in each individual experiment.

Titration of Oligomycin, FCCP, and Rot/AA in Human Hepatocytes

The study was performed on the Seahorse XF HS mini Analyzer (Agilent Technology, Cedar Creek, TX). In our initial experiment using the Seahorse XFp Cell Mito Stress Test Kit (103010-100; Agilent Technology), the doses recommended by the manufacturer were not enough to induce the full effect of the drugs. Thus, we performed a titration experiment of all 3 drugs to optimize doses to study mitochondrial functions and respiration. Hepatocytes were seeded in the miniplate (103025-100; Agilent Technology) wells B-G (wells A and H were left as blank controls) at a density of 40,000 cells per well and were cultured in a regular (lean) medium for 7 days before the titration study. The 4 injection ports were loaded with each of 3 drugs of the step concentration indicated in Table 6 in a hydrated cartridge. The titration protocol was performed and consisted of an equilibration period, a basal OCR measurement with 3 cycles and 6-minute intervals, and 4 OCR measurements after an injection each with 3 cycles and 6-minute intervals. The final accumulative concentration was chosen as the optimized dose of the drug when the curve reached a plateau phase and was used in the following studies.

Measurement of Mitochondrial Functions and Respiration

Hepatocytes were seeded at a density of 40,000 cells per well in wells B-G on the miniplates, and wells A and H were left as blank controls. A side-by-side comparison was made between 7L vs 7F or 14L vs 7F7L in triplicate on the same miniplate. After the completion of their corresponding timelines, hepatocytes were cultured in XF Dulbecco's modified Eagle medium (103575-100; Agilent Technology) supplied with 10 mmol/L glucose (103577-100; Agilent Technology), 1 mmol/L pyruvate (103578-100; Agilent Technology), and 2 mmol/L L-glutamine (103579-100; Agilent Technology) for 1 hour in a non-CO₂ 37°C incubator. Solutions (10×) were made for oligomycin (200 μ mol/L), FCCP (80 μ mol/L), and Rot/AA (50 μ mol/L) as optimized final concentrations based on the earlier titration experiment and loaded to injection ports A-C on a hydrated cartridge. Subsequently, the XFp Cell Mito Stress Test protocol was executed on the Seahorse XF HS mini Analyzer. The protocol consisted of an equilibration period, basal OCR measurement (3 cycles, 6-minute interval), and 3 OCR measurements after drug injections each with 3 cycles and 6-minute intervals.

In Vitro H₂O₂ Dose-Response Assay and Viability

Hepatocytes were seeded on 96-well plates at a density of 40,000 cells per well. After the completion of their corresponding timelines, hepatocytes were cultured in a regular (lean) medium supplied with H_2O_2 of a range of concentrations of 0, 50, 100, 500, 1000, 5000, 10,000, and

 $50,000~\mu\text{mol/L}$ and cultured for 24 hours. Subsequently, hepatocytes were subjected to viability measurements using a 3-(4,5-dimethylthiazol-2-yl)-2,5-diphenyltetrazolium bromide assay (V13154; Invitrogen) in accord with the manufacturer's instructions, measurement was performed using a plate reader for absorbance at 570 nm.

Statistical Analysis

Data are presented as means \pm SD (unless indicated otherwise) in Tables 1–4 in a donor-specific fashion and collectively in Figures. A 2-way, repeated-measure analysis of variance followed by Tukey multiple comparisons to test the difference among groups subjected to different treatment (lean vs fatty) and for a different length of time (7 vs 14 days). A P value less than .05 was considered an indication of statistical significance. Statistical analyses were performed using GraphPad Prism (GraphPad Software, www.graphpad.com). All authors had access to the study data and reviewed and approved the final manuscript.

References

- Mikolasevic I, Milic S, Wensveen TT, Grgic I, Jakopcic I, Stimac D, Wensveen F, Orlic L. Nonalcoholic fatty liver disease-a multisystem disease? World J Gastroenterol 2016;22:9488.
- Geisler CE, Renquist BJ. Hepatic lipid accumulation: cause and consequence of dysregulated glucoregulatory hormones. J Endocrinol 2017;234:R1–R21.
- Younossi ZM, Blissett D, Blissett R, Henry L, Stepanova M, Younossi Y, Racila A, Hunt S, Beckerman R. The economic and clinical burden of nonalcoholic fatty liver disease in the United States and Europe. Hepatology 2016;64:1577–1586.
- Huang DQ, El-Serag HB, Loomba R. Global epidemiology of NAFLD-related HCC: trends, predictions, risk factors and prevention. Nat Rev Gastroenterol Hepatol 2021;18:223–238.
- Fisher CD, Jackson JP, Lickteig AJ, Augustine LM, Cherrington NJ. Drug metabolizing enzyme induction pathways in experimental non-alcoholic steatohepatitis. Arch Toxicol 2008;82:959–964.
- Eslam M, Sanyal AJ, George J, Sanyal A, Neuschwander-Tetri B, Tiribelli C, Kleiner DE, Brunt E, Bugianesi E, Yki-Järvinen H. MAFLD: a consensus-driven proposed nomenclature for metabolic associated fatty liver disease. Gastroenterology 2020;158:1999–2014. e1.
- Reynaert H, Geerts A, Henrion J. The treatment of nonalcoholic steatohepatitis with thiazolidinediones. Aliment Pharmacol Ther 2005;22:897–905.
- 8. Wieckowska A, Feldstein AE. Diagnosis of nonalcoholic fatty liver disease: invasive versus noninvasive. Semin Liver Dis 2008;28:386–395.
- Younossi ZM, Koenig AB, Abdelatif D, Fazel Y, Henry L, Wymer M. Global epidemiology of nonalcoholic fatty liver disease—meta-analytic assessment of prevalence, incidence, and outcomes. Hepatology 2016;64:73–84.
- 10. Li J, Zou B, Yeo YH, Feng Y, Xie X, Lee DH, Fujii H, Wu Y, Kam LY, Ji F. Prevalence, incidence, and outcome of

- non-alcoholic fatty liver disease in Asia, 1999–2019: a systematic review and meta-analysis. Lancet Gastroenterol Hepatol 2019;4:389–398.
- 11. Rolo AP, Teodoro JS, Palmeira CM. Role of oxidative stress in the pathogenesis of nonalcoholic steatohepatitis. Free Radic Biol Med 2012;52:59–69.
- Serviddio G, Bellanti F, Vendemiale G. Free radical biology for medicine: learning from nonalcoholic fatty liver disease. Free Radic Biol Med 2013;65:952–968.
- Day CP, James OF. Steatohepatitis: a tale of two "hits"? Elsevier, 1998.
- 14. Buzzetti E, Pinzani M, Tsochatzis EA. The multiple-hit pathogenesis of non-alcoholic fatty liver disease (NAFLD). Metabolism 2016;65:1038–1048.
- Paschos P, Paletas K. Non alcoholic fatty liver disease two-hit process: multifactorial character of the second hit. Hippokratia 2009;13:128.
- Zarghamravanbakhsh P, Frenkel M, Poretsky L. Metabolic causes and consequences of nonalcoholic fatty liver disease (NAFLD). Metabol Open 2021;12:100149.
- 17. Chen Z, Yu Y, Cai J, Li H. Emerging molecular targets for treatment of nonalcoholic fatty liver disease. Trends Endocrinol Metab 2019;30:903–914.
- Koliaki C, Szendroedi J, Kaul K, Jelenik T, Nowotny P, Jankowiak F, Herder C, Carstensen M, Krausch M, Knoefel WT. Adaptation of hepatic mitochondrial function in humans with non-alcoholic fatty liver is lost in steatohepatitis. Cell Metab 2015;21:739–746.
- Sunny NE, Parks EJ, Browning JD, Burgess SC. Excessive hepatic mitochondrial TCA cycle and gluconeogenesis in humans with nonalcoholic fatty liver disease. Cell Metab 2011;14:804–810.
- Nunnari J, Suomalainen A. Mitochondria: in sickness and in health. Cell 2012:148:1145–1159.
- Rauckhorst AJ, Gray LR, Sheldon RD, Fu X, Pewa AD, Feddersen CR, Dupuy AJ, Gibson-Corley KN, Cox JE, Burgess SC. The mitochondrial pyruvate carrier mediates high fat diet-induced increases in hepatic TCA cycle capacity. Mol Metab 2017;6:1468–1479.
- 22. Satapati S, Kucejova B, Duarte JA, Fletcher JA, Reynolds L, Sunny NE, He T, Nair LA, Livingston K, Fu X. Mitochondrial metabolism mediates oxidative stress and inflammation in fatty liver. J Clin Invest 2015;125:4447–4462.
- 23. Caldwell SH, Swerdlow RH, Khan EM, lezzoni JC, Hespenheide EE, Parks JK, Parker WD Jr. Mitochondrial abnormalities in non-alcoholic steatohepatitis. J Hepatol 1999;31:430–434.
- Sanyal AJ, Campbell–Sargent C, Mirshahi F, Rizzo WB, Contos MJ, Sterling RK, Luketic VA, Shiffman ML, Clore JN. Nonalcoholic steatohepatitis: association of insulin resistance and mitochondrial abnormalities. Gastroenterology 2001;120:1183–1192.
- 25. Cortez-Pinto H, Chatham J, Chacko V, Arnold C, Rashid A, Diehl AM. Alterations in liver ATP homeostasis in human nonalcoholic steatohepatitis: a pilot study. JAMA 1999;282:1659–1664.
- Berthiaume F, Barbe L, Mokuno Y, MacDonald AD, Jindal R, Yarmush ML. Steatosis reversibly increases hepatocyte sensitivity to hypoxia-reoxygenation injury. J Surg Res 2009;152:54–60.

- Pirola CJ, Gianotti TF, Burgueño AL, Rey-Funes M, Loidl CF, Mallardi P, San Martino J, Castaño GO, Sookoian S. Epigenetic modification of liver mitochondrial DNA is associated with histological severity of nonalcoholic fatty liver disease. Gut 2013;62:1356–1363.
- Demeilliers C, Maisonneuve C, Grodet A, Mansouri A, Nguyen R, Tinel M, Lettéron P, Degott C, Feldmann G, Pessayre D. Impaired adaptive resynthesis and prolonged depletion of hepatic mitochondrial DNA after repeated alcohol binges in mice. Gastroenterology 2002; 123:1278–1290.
- Moore AS, Holzbaur EL. Mitochondrial-cytoskeletal interactions: dynamic associations that facilitate network function and remodeling. Curr Opin Physiol 2018; 3:94–100.
- Pekkurnaz G, Trinidad JC, Wang X, Kong D, Schwarz TL. Glucose regulates mitochondrial motility via Milton modification by O-GlcNAc transferase. Cell 2014; 158:54–68.
- 31. Sukhorukov VM, Meyer-Hermann M. Structural heterogeneity of mitochondria induced by the microtubule cytoskeleton. Sci Rep 2015;5:1–13.
- **32.** Schwarz TL. Mitochondrial trafficking in neurons. Cold Spring Harb Perspect Biol 2013;5:a011304.
- 33. Park C, Lee S-A, Hong J-H, Suh Y, Park SJ, Suh BK, Woo Y, Choi J, Huh J-W, Kim Y-M. Disrupted-in-schizophrenia 1 (DISC1) and Syntaphilin collaborate to modulate axonal mitochondrial anchoring. Mol Brain 2016;9:1–11.
- 34. Ashrafi G, Schlehe JS, LaVoie MJ, Schwarz TL. Mitophagy of damaged mitochondria occurs locally in distal neuronal axons and requires PINK1 and Parkin. J Cell Biol 2014;206:655–670.
- Lin M-Y, Cheng X-T, Tammineni P, Xie Y, Zhou B, Cai Q, Sheng Z-H. Releasing syntaphilin removes stressed mitochondria from axons independent of mitophagy under pathophysiological conditions. Neuron 2017; 94:595–610. e6.
- Quintero OA, DiVito MM, Adikes RC, Kortan MB, Case LB, Lier AJ, Panaretos NS, Slater SQ, Rengarajan M, Feliu M. Human Myo19 is a novel myosin that associates with mitochondria. Curr Biol 2009; 19:2008–2013.
- Pathak D, Sepp KJ, Hollenbeck PJ. Evidence that myosin activity opposes microtubule-based axonal transport of mitochondria. J Neurosci 2010; 30:8984–8992.
- 38. Moore AS, Wong YC, Simpson CL, Holzbaur EL. Dynamic actin cycling through mitochondrial subpopulations locally regulates the fission–fusion balance within mitochondrial networks. Nat Commun 2016;7:1–13.
- Korobova F, Ramabhadran V, Higgs HN. An actindependent step in mitochondrial fission mediated by the ER-associated formin INF2. Science 2013; 339:464–467.
- Manor U, Bartholomew S, Golani G, Christenson E, Kozlov M, Higgs H, Spudich J, Lippincott-Schwartz J. A mitochondria-anchored isoform of the actin-nucleating spire protein regulates mitochondrial division. Elife 2015; 4:e08828.

- Li S, Xu S, Roelofs BA, Boyman L, Lederer WJ, Sesaki H, Karbowski M. Transient assembly of F-actin on the outer mitochondrial membrane contributes to mitochondrial fission. J Cell Biol 2015;208:109–123.
- Miragoli M, Sanchez-Alonso JL, Bhargava A, Wright PT, Sikkel M, Schobesberger S, Diakonov I, Novak P, Castaldi A, Cattaneo P. Microtubule-dependent mitochondria alignment regulates calcium release in response to nanomechanical stimulus in heart myocytes. Cell Rep 2016;14:140–151.
- Schulze RJ, Schott MB, Casey CA, Tuma PL, McNiven MA. The cell biology of the hepatocyte: a membrane trafficking machine. J Cell Biol 2019; 218:2096–2112.
- Shepard BD, Tuma PL. Alcohol-induced alterations of the hepatocyte cytoskeleton. World J Gastroenterol 2010;16:1358.
- Neuschwander-Tetri BA. Lifestyle modification as the primary treatment of NASH. Clin Liver Dis 2009; 13:649–665.
- 46. Johnson NA, George J. Fitness versus fatness: moving beyond weight loss in nonalcoholic fatty liver disease. Hepatology 2010;52:370–380.
- Vilar-Gomez E, Martinez-Perez Y, Calzadilla-Bertot L, Torres-Gonzalez A, Gra-Oramas B, Gonzalez-Fabian L, Friedman SL, Diago M, Romero-Gomez M. Weight loss through lifestyle modification significantly reduces features of nonalcoholic steatohepatitis. Gastroenterology 2015;149:367–378. e5.
- Berthiaume F, Moghe PV, Toner M, Yarmush ML. Effect of extracellular matrix topology on cell structure, function, and physiological responsiveness: hepatocytes cultured in a sandwich configuration. FASEB J 1996; 10:1471–1484.
- Wake K, Sato T. "The sinusoid" in the liver: lessons learned from the original definition by Charles Sedgwick Minot (1900). Anat Rec 2015;298:2071–2080.
- Dunn JC, Yarmush ML, Koebe HG, Tompkins RG. Hepatocyte function and extracellular matrix geometry: long-term culture in a sandwich configuration. FASEB J 1989;3:174–177.
- Sidhu JS, Farin FM, Omiecinski CJ. Influence of extracellular matrix overlay on phenobarbital-mediated induction of CYP2B1, 2B2, and 3A1 genes in primary adult rat hepatocyte culture. Arch Biochem Biophys 1993; 301:103–113.
- 52. Musat Al, Sattler CA, Sattler GL, Pitot HC. Reestablishment of cell polarity of rat hepatocytes in primary culture. Hepatology 1993;18:198–205.
- Dunn JC, Tompkins RG, Yarmush ML. Long-term in vitro function of adult hepatocytes in a collagen sandwich configuration. Biotechnol Prog 1991;7:237–245.
- Ezzell RM, Toner M, Hendricks K, Dunn JC, Tompkins RG, Yarmush ML. Effect of collagen gel configuration on the cytoskeleton in cultured rat hepatocytes. Exp Cell Res 1993;208:442–452.
- LeCluyse EL, Audus KL, Hochman JH. Formation of extensive canalicular networks by rat hepatocytes cultured in collagen-sandwich configuration. Am J Physiol Cell Physiol 1994;266:C1764–C1774.

- 56. Rey-Bedon C, Banik P, Gokaltun A, Hofheinz O, Yarmush ML, Uygun MK, Usta OB. CYP450 drug inducibility in NAFLD via an in vitro hepatic model: understanding drug-drug interactions in the fatty liver. Biomed Pharmacother 2022;146:112377.
- Bretscher A. Microfilament structure and function in the cortical cytoskeleton. Ann Rev Cell Biol 1991;7:337–374.
- Mays RW, Beck KA, Nelson WJ. Organization and function of the cytoskeleton in polarized epithelial cells: a component of the protein sorting machinery. Curr Opin Cell Biol 1994;6:16–24.
- Tuma DJ, Smith TE, Schaffert CS, Kharbanda KK, Sorrell MF. Ethanol feeding selectively impairs the spreading of rat perivenous hepatocytes on extracellular matrix substrates. Alcohol Clin Exp Res 1999; 23:1673–1680.
- Schaffert CS, Sorrell MF, Tuma DJ. Expression and cytoskeletal association of integrin subunits is selectively increased in rat perivenous hepatocytes after chronic ethanol administration. Alcohol Clin Exp Res 2001; 25:1749–1757.
- Meads T, Schroer TA. Polarity and nucleation of microtubules in polarized epithelial cells. Cell Motil Cytoskeleton 1995;32:273–288.
- 62. Tuma DJ, Smith SL, Sorrell MF. Acetaldehyde and microtubules. Ann N Y Acad Sci 1991;625:786–792.
- 63. Jennett RB, Sorrell MF, Saffar-Fard A, Ockner JL, Tuma DJ. Preferential covalent binding of acetaldehyde to the α -chain of purified rat liver tubulin. Hepatology 1989;9:57–62.
- 64. Jennett R, Sorrell M, Johnson E, Tuma D. Covalent binding of acetaldehyde to tubulin: evidence for preferential binding to the α -chain. Arch Biochem Biophys 1987;256:10–18.
- 65. Jennett RB, Tuma DJ, Sorrell MF. Effect of ethanol and its metabolites on microtubule formation. Pharmacology 1980;21:363–368.
- Tuma DJ, Carol CA, Sorrell MF. Effects of ethanol on hepatic protein trafficking: impairment of receptormediated endocytosis. Alcohol Alcohol 1990; 25:117–125.
- McVicker BL, Casey CA. Effects of ethanol on receptormediated endocytosis in the liver. Alcohol 1999; 19:255–260.
- 68. Schaffert CS, Todero SL, Casey CA, Thiele GM, Sorrell MF, Tuma DJ. Chronic ethanol treatment impairs Rac and Cdc42 activation in rat hepatocytes. Alcohol Clin Exp Res 2006;30:1208–1213.
- 69. lozzo P, Bucci M, Roivainen A, Någren K, Järvisalo MJ, Kiss J, Guiducci L, Fielding B, Naum AG, Borra R. Fatty acid metabolism in the liver, measured by positron emission tomography, is increased in obese individuals. Gastroenterology 2010;139:846–856. e6.
- Brady L, Brady P, Romsos D, Hoppel C. Elevated hepatic mitochondrial and peroxisomal oxidative capacities in fed and starved adult obese (ob/ob) mice. Biochem J 1985;231:439–444.
- McCune SA, Durant PJ, Jenkins PA, Harris RA. Comparative studies on fatty acid synthesis, glycogen metabolism, and gluconeogenesis by hepatocytes

- isolated from lean and obese Zucker rats. Metabolism 1981;30:1170–1178.
- Pérez-Carreras M, Del Hoyo P, Martín MA, Rubio JC, Martín A, Castellano G, Colina F, Arenas Jn, Solis-Herruzo JA. Defective hepatic mitochondrial respiratory chain in patients with nonalcoholic steatohepatitis. Hepatology 2003;38:999–1007.
- 73. Nativ NI, Yarmush G, So A, Barminko J, Maguire TJ, Schloss R, Berthiaume F, Yarmush ML. Elevated sensitivity of macrosteatotic hepatocytes to hypoxia/reoxygenation stress is reversed by a novel defatting protocol. Liver Transplant 2014;20:1000–1011.
- Videla LA, Rodrigo R, Orellana M, Fernandez V, Tapia G, Quiñones L, Varela N, Contreras J, Lazarte R, Csendes A. Oxidative stress-related parameters in the liver of non-alcoholic fatty liver disease patients. Clin Sci 2004;106:261–268.
- Gornicka A, Morris-Stiff G, Thapaliya S, Papouchado BG, Berk M, Feldstein AE. Transcriptional profile of genes involved in oxidative stress and antioxidant defense in a dietary murine model of steatohepatitis. Antioxid Redox Signal 2011;15:437–445.
- Mantena SK, Vaughn DP Jr, Andringa KK, Eccleston HB, King AL, Abrams GA, Doeller JE, Kraus DW, Darley-Usmar VM, Bailey SM. High fat diet induces dysregulation of hepatic oxygen gradients and mitochondrial function in vivo. Biochem J 2009;417:183–193.
- Chacko BK, Zhi D, Darley-Usmar VM, Mitchell T. The Bioenergetic Health Index is a sensitive measure of oxidative stress in human monocytes. Redox Biol 2016; 8:43–50.
- Young CK, Young MJ. Comparison of HepaRG cells following growth in proliferative and differentiated culture conditions reveals distinct bioenergetic profiles. Cell Cycle 2019;18:476–499.
- 79. Dahl C, Guldberg P, Abildgaard C. Evaluating the role of RAR β signaling on cellular metabolism in melanoma using the Seahorse XF analyzer. Retinoid and rexinoid signaling. Springer, 2019:171–180.
- Campioni G, Pasquale V, Busti S, Ducci G, Sacco E, Vanoni M. An optimized workflow for the analysis of metabolic fluxes in cancer spheroids using Seahorse technology. Cells 2022;11:866.
- 81. Shen Y, Yang J, Li J, Shi X, Ouyang L, Tian Y, Lu J. Carnosine inhibits the proliferation of human gastric cancer SGC-7901 cells through both of the mitochondrial respiration and glycolysis pathways. PLoS One 2014;9:e104632.
- **82.** Degli Esposti D, Hamelin J, Bosselut N, Saffroy R, Sebagh M, Pommier A, Martel C, Lemoine A. Mitochondrial roles and cytoprotection in chronic liver injury. Biochem Res Int 2012;2012:387626.
- 83. An P, Wei L-L, Zhao S, Sverdlov DY, Vaid KA, Miyamoto M, Kuramitsu K, Lai M, Popov YV. Hepatocyte mitochondria-derived danger signals directly activate hepatic stellate cells and drive progression of liver fibrosis. Nat Commun 2020;11:1–15.
- 84. Robin ED, Wong R. Mitochondrial DNA molecules and virtual number of mitochondria per cell in mammalian cells. J Cell Physiol 1988;136:507–513.

- 85. Kim T-Y, Wang D, Kim AK, Lau E, Lin AJ, Liem DA, Zhang J, Zong NC, Lam MP, Ping P. Metabolic labeling reveals proteome dynamics of mouse mitochondria. Mol Cell Proteomics 2012;11:1586–1594.
- **86.** Miwa S, Lawless C, Von Zglinicki T. Mitochondrial turnover in liver is fast in vivo and is accelerated by dietary restriction: application of a simple dynamic model. Aging Cell 2008;7:920–923.
- 87. Vona R, Mileo AM, Matarrese P. Microtubule-based mitochondrial dynamics as a valuable therapeutic target in cancer. Cancers (Basel) 2021;13:5812.
- 88. Cho MJ, Kim YJ, Yu WD, Kim YS, Lee JH. Microtubule integrity is associated with the functional activity of mitochondria in HEK293. Cells 2021;10:3600.
- 89. Shum M, Ngo J, Shirihai OS, Liesa M. Mitochondrial oxidative function in NAFLD: friend or foe? Mol Metab 2021;50:101134.
- Begriche K, Massart J, Robin MA, Bonnet F, Fromenty B. Mitochondrial adaptations and dysfunctions in nonalcoholic fatty liver disease. Hepatology 2013;58:1497–1507.
- Sunny NE, Bril F, Cusi K. Mitochondrial adaptation in nonalcoholic fatty liver disease: novel mechanisms and treatment strategies. Trends Endocrinol Metab 2017; 28:250–260.

Received August 30, 2022. Accepted April 4, 2023.

Correspondence

Address correspondence to: O. Berk Usta, PhD, Department of Surgery, Massachusetts General Hospital, 51 Blossom Street, Boston, Massachusetts 02114. e-mail: ousta@mgh.harvard.edu; berkusta@gmail.com.

Acknowledgments

The authors express their most sincere gratitude to the Cell Resource Core for providing the human hepatocytes and to Dr Dennis Brown and Dr Richard Bouley for their support in confocal microscopy at the Microscopy Core for the Program in Membrane Biology at Massachusetts General Hospital. The authors also acknowledge the support and use of facilities at the Morphology and Imaging Shared Facility, and Regenerative Medicine Shared Facility provided at the Shriners Hospital for Children–Boston.

CRediT Authorship Contributions

Letao FAN, PhD (Conceptualization: Lead; Formal analysis: Lead; Investigation: Lead; Methodology: Lead; Validation: Lead; Visualization: Lead; Writing – original draft: Lead; Writing – review & editing: Lead)

Aslinan Gokaltun, PhD (Investigation: Supporting; Methodology: Supporting; Validation: Supporting; Writing – review & editing: Supporting)

Sarah Maggipinto, BS (Investigation: Supporting; Methodology: Supporting; Validation: Supporting; Writing – review & editing: Supporting)

Yoshinori Kitagawa, MD, PhD (Investigation: Supporting; Methodology: Supporting; Validation: Supporting; Writing – review & editing: Supporting)

Jeevendra Martyn, MD (Resources: Supporting; Writing – review & editing: Supporting)

Heidi YEH, MD (Conceptualization: Supporting; Writing – review & editing: Supporting)

Basak E. Uygun, PhD (Conceptualization: Supporting; Resources: Supporting; Supervision: Supporting; Writing – review & editing: Supporting) Martin Leon Yarmush, MD, PhD (Conceptualization: Equal; Methodology:

Martin Leon Yarmush, MD, PhD (Conceptualization: Equal; Methodology: Equal; Resources: Equal; Supervision: Supporting; Writing – review & editing: Supporting)

Osman Berk USTA, PhD (Conceptualization: Equal; Formal analysis: Supporting; Funding acquisition: Lead; Methodology: Equal; Project administration: Lead; Supervision: Lead; Writing – original draft: Equal; Writing – review & editing: Equal)

Conflicts of interest

The authors disclose no conflicts.

Funding

This research was supported partially by grants from the National Institutes of Health (5R21GM136002, 1R21GM 141683, 1R21GM140656, and 5R01HL145031) for O.B.U, L.F, A.G and M.L.Y, National Science Foundation (1941543) for O.B.U, A.G. and M.L.Y., and a Massachusetts General Hospital Executive Committee on Research Interim Support Fund for O. B.U.